Numerical-relativity simulations of long-lived remnants of binary neutron star mergers

Roberto De Pietri,[1,2] Alessandra Feo,[3,2] José A. Font,[4,5] Frank Löffler,[6,7] Michele Pasquali,[1,2] and Nikolaos Stergioulas[8]

[1]*Parma University, Parco Area delle Scienze 7/A, I-43124 Parma (PR), Italy*
[2]*INFN gruppo collegato di Parma, Parco Area delle Scienze 7/A, I-43124 Parma (PR), Italy*
[3]*Department of Chemistry, Life Sciences and Environmental Sustainability, Parma University, Parco Area delle Scienze, 157/A, I-43124 Parma (PR), Italy*
[4]*Departamento de Astronomía y Astrofísica, Universitat de València, Dr. Moliner 50, 46100, Burjassot (València), Spain*
[5]*Observatori Astronòmic, Universitat de València, C/ Catedrático José Beltrán 2, 46980, Paterna (València), Spain*
[6]*Heinz Nixdorf Chair for Distributed Information Systems, Friedrich Schiller University Jena, Jena, Germany*
[7]*Center for Computation & Technology, Louisiana State University, Baton Rouge, Louisiana 70803 USA*
[8]*Department of Physics, Aristotle University of Thessaloniki, Thessaloniki 54124, Greece*

(Received 10 October 2019; accepted 28 February 2020; published 24 March 2020)

We analyze the properties of the gravitational wave signal emitted after the merger of a binary neutron star system when the remnant survives for more than a 80 ms (and up to 140 ms). We employ four different piecewise polytropic equations of state supplemented by an ideal fluid thermal component. We find that the postmerger phase can be subdivided into three phases: an early postmerger phase (where the quadrupole mode and a few subdominant features are active), the intermediate postmerger phase (where only the quadrupole mode is active) and the late postmerger phase (where convective instabilities trigger inertial modes). The inertial modes have frequencies somewhat smaller than the quadrupole modes. In one model, we find an interesting association of a corotation of the quadrupole mode in parts of the star with a revival of its amplitude. The gravitational wave emission of inertial modes in the late postmerger phase is concentrated in a narrow frequency region and is potentially detectable by the planned third-generation detectors. This allows for the possibility of probing not only the cold part of the equation of state, but also its dependence on finite temperature. In view of these results, it will be important to investigate the impact of various type of viscosities on the potential excitation of inertial modes in binary neutron star merger remnants.

DOI: 10.1103/PhysRevD.101.064052

I. INTRODUCTION

The landmark joint detection of gravitational waves (GWs) and electromagnetic waves from the binary neutron star merger event GW170817 / GRB 170817A / AT 2017gfo is widely regarded as the start of multi-messenger astrophysics (see [1] and references therein). This unique event has provided key evidence to address long-standing issues in relativistic astrophysics such as the origin of short gamma-ray bursts and kilonovae, the *r*-process-mediated nucleosynthesis of heavy elements, and independent measures of cosmological parameters [2–5]. Constraints on the binary parameters, such as component masses, radii, spins, and the equation of state (EOS), as derived from the detected GW signal in the inspiral phase, were first presented in [6] and subsequently improved in [7,8]. See also [9–12] for additional estimates, [13] for a different assessment of EOS constraints, and [14,15] for future prospects. The constraints on radii and EOS are based on the analysis of the tidal interactions between the two stars during their inspiral. Additional constraints on the radius can be obtained assuming that there was no prompt collapse of the remnant (see, e.g., [16] and [17,18] for reviews and references therein). Complementary information on the internal structure of neutron stars is expected to become available through the observation of the post-merger GW signal, primarily through the application of an empirical relation between the $m = 2$ f-mode frequency and the neutron star radius (see, e.g., [19–31] and [17,18] for reviews and references therein). A first potential approach for inferring information on the finite-temperature dependence of the EOS, based on the long-term GW emission in the postmerger phase, was presented in [32].

Reliable theoretical models of postmerger GW emission can only be obtained through nonlinear, general-relativistic numerical simulations. Generically, such numerical simulations of binary neutron star (BNS) mergers show that the outcome depends on the component masses and the EOS (see e.g., [33–36] for reviews). Prompt collapse to a black hole is the likely outcome only if the initial masses are sufficiently large, while delayed collapse (or no collapse) is produced otherwise. In the latter cases, the resulting object may be either a hypermassive neutron star (HMNS) [37], where the remnant is temporarily supported against collapse by differential rotation and thermal gradients, or even a supramassive neutron star, when the mass of the remnant is sufficiently small to be supported by rigid rotation [38]. Either case leads to sufficiently long-lived remnants to produce large amounts of high-frequency (∼kHz) gravitational radiation. Hypermassive remnants may avoid collapse for timescales of tens to hundreds of milliseconds. Supramassive neutron stars will avoid collapse on an immensely longer timescale set by magnetic dipole radiation. On such long timescales, additional GW emission mechanisms may become relevant, such as the Chandrasekhar-Friedman-Schutz (CFS) instability [39,40], shear instabilities [41–43] or convective instabilities in rotating stars with nonbarotropic thermal profiles [44]. There is thus good reason to study in more detail the long-term evolution of BNS remnants.

Due to their high frequency, the GW signals produced by postmerger remnants are much more difficult to detect for the Advanced LIGO and Virgo detectors than those from the late inspiral phase, as the (quantum) shot-noise limits the sensitivity of interferometers above a few kHz. Not surprisingly, the recent searches for GWs from the postmerger remnant conducted by the LIGO/Virgo collaboration in the data of GW170817 have not revealed any detection [45–47]. Nevertheless, postmerger GWs for GW170817-like events, in terms of distance and amplitude, seem within reach of future observing runs with expected higher sensitivity. We note that a seconds-long postmerger signal candidate has been reported by [48] with a lower GW energy estimate than that computed by [45].

Simulations of the postmerger phase of HMNSs show the emission of significant amounts of gravitational radiation at distinct frequencies of a few kHz (e.g., [19,21–24,49–62]), with contributions as low as ∼1 kHz, depending on the EOS [63], see [64] for a review and references therein. All of these simulations last for up to a few tens of ms after merger, which is long enough to show that the GW emission is dominated by a main peak in the frequency range ∼2–4 kHz, with secondary peaks on both sides of the main peak. Employing a mode-analysis technique it was found in [21], that the main postmerger peak is due to the excitation of the fundamental $m = 2$ f-mode (denoted in the literature as or $f_{\rm peak}$ or f_2). In addition, it was shown in [21] that some of the secondary peaks can be explained as a quasilinear combinations between f_2 and the fundamental, quasiradial, $m = 0$ mode (that is, sums and differences of these frequencies, denoted, e.g., as f_{2-0} and f_{2+0}). These combination frequencies are primarily present in models that are relatively close to the threshold mass to collapse (high-mass/soft EOS models) [24]. In addition, in [24] it was found that a different secondary peak, $f_{\rm spiral}$, is present in models that are relatively far from the threshold mass to collapse (low-mass/stiff EOS) and it is due to a spiral deformation excited during merger. Depending on the relative strength between f_{2-0} and $f_{\rm spiral}$, [24] introduced a spectral classification of the postmerger GW emission (see [17,28] for reviews). For additional studies of the properties of postmerger remnants (where sometimes a different label for the mode is used), see e.g., [56,61,63,65–76] as well as [18] and references therein.

Recently we performed numerical simulations in full general relativity of BNS systems, extending the simulation time significantly longer than those previously reported in the literature [32]. These simulations allowed us to find new features in the GW spectrum of the remnant on longer timescales. In particular, the simulations were extended up to ∼140 ms after merger and were based on a piecewise polytropic approximation for the EOS treatment, supplemented by a thermal component. We found that after an initial phase of a few tens of ms (where the dominant oscillation mode of the remnant and main GW emitter is the $m = 2$ f-mode), convective instabilities in the remnant may excite inertial modes, which also radiate GWs. The phase during which inertial modes of global and discrete nature can be excited, may last at least up to several tens of milliseconds and, as shown in [32], the associated GW emission may become potentially observable by the planned third-generation GW detectors at frequencies of a few kHz.

Here, we complement the study initiated in [32] by carrying out the analysis of additional simulations, which account for two new EOS, namely H4 and MS1. Within the range of validity of the input physics and assumptions employed in our simulations, the extended results presented here confirm our earlier findings in a generic way. we present a convergence check for a specific model to further validate our results.

The paper is organized as follows: in Sec. II we discuss our initial models and numerical setup. Section III presents our main results, with a particular attention to the mode analysis in Secs. III B–III E. A summary of the main results presented in the previous sections of this work is provided in Sec. IV. The paper closes with three Appendixes, where numerical issues and convergence properties of our simulations are discussed (Appendix A), along with a revision of past literature regarding long-term simulations of the postmerger phase of binary neutron star mergers (Appendix B), and the thermodynamical properties of the piecewise-polytropic EOS used in this study (Appendix C).

Unless otherwise noted, we employ units of $c = G = M_\odot = 1$.

II. INITIAL DATA AND SETUP

Initial data for irrotational neutron star binaries in the conformal thin sandwich approximation are generated using the LORENE code [77,78]. We employ four EOS, namely SLy, APR4, H4, and MS1, parametrized as piecewise polytropes [79] with 7 pieces plus a thermal component with adiabatic index $\Gamma_{\rm th} = 1.8$. The main properties of our initial data (see. Table I) are a total baryonic mass of 2.8 $M_\odot$ and a total mass of $\simeq$2.55–2.60 $M_\odot$ with an initial separation of $\approx$44.3 km (four full orbits before merger). We consider equal-mass systems characterized by relatively low-mass components, below the range of the inferred masses for GW170817 [7] (which had a total mass between 2.73 $M_\odot$ for low-spin priors and 2.77 $M_\odot$ for high-spin priors).

The initial data are evolved using the EINSTEIN TOOLKIT [80], an open source, modular code for numerical relativity based on the Cactus framework [81,82]. For the simulations we employ the same setting in the code as in [63,69,83–85]. The only difference here is the use of π-symmetry to reduce the computational cost by a factor 2. This allows to push the limit of the simulated time to $\sim$150 ms, of which the last 130 ms correspond to the postmerger phase.

The set of equations we solve numerically comprise Einstein's gravitational field equations, the general relativistic hydrodynamics equations for a perfect-fluid stress-energy tensor and the relativistic energy conservation equation. Therefore, our simulations do not account for effects due to magnetic fields or nonthermal radiation transport associated with neutrinos. In particular, we evolve Einstein's equations in the BSSN formulation [86,87], as implemented in the McLachlan module [88], and the Valencia formulation of the general relativistic hydrodynamics equations [89,90], as implemented in the public GRHydro module [91,92]. For the matter fields we employ a finite-volume algorithm with the HLLE Riemann solver [93,94] and the WENO reconstruction method [95,96]. The combined use of WENO reconstruction and the BSSN formulation was found in [69] to be the best combination within the EINSTEIN TOOLKIT even at low resolution. For the time evolution we used the Method of Lines with a fourth-order, conservative Runge-Kutta scheme [97,98]. The evolved variables for both the spacetime and the hydrodynamics are discretized on a Cartesian grid with 6 levels of fixed mesh refinement, each using twice the resolution of its parent level. The outermost boundary of the grid is set at 720 $M_\odot$ ($\approx$1040 km) from the center. The standard spatial resolution at the finest refinement level in our production runs is $dx = 277$ m. For the SLy EOS, we also use a higher-resolution setup, with spatial resolution at the finest level of $dx = 185$ m (this simulation is denoted as SLy HR below). A comparison of GW spectrograms for the two resolutions is provided in Appendix A.

III. RESULTS

A. Matter dynamics and waveforms

The dynamics of the matter of the four models considered in this work can be followed by analyzing the time evolution of quantities such as the central density and the density distribution within the equatorial and the vertical planes. The overall behavior for the first phase (inspiral and merger) of the binary system's evolution is similar for each model, until the two neutron stars form a bar-deformed remnant as in [69] (the appearance of a bar deformation is due to the rotating pattern of the dominant $m = 2$ f-mode excited after merger). During the initial postmerger phase we note some oscillations in the evolution of the maximum density, as shown in Fig. 1, which have different durations for each model. For the SLy and MS1 EOS these oscillations last $\sim$7 ms while for the APR4 and H4 ~ 4 and $\sim$5 ms respectively, until the core becomes more stable and the bar-deformed remnant is left. This configuration of a bar-deformed remnant survives for some tens of milliseconds for each model before becoming nearly axisymmetric and more stable.

We note that for the SLy and H4 EOS the density of the core grows even after the oscillations in the maximum density have dampened (see Sec. III B for a discussion of the frequency evolution of the dominant $m = 2$ f-mode during this time interval). Eventually, a delayed collapse to a black hole occurs for both of these two models, at $\sim$124 and $\sim$84 ms after the merger, respectively, while we do not observe a collapse to a black hole in the case of APR4 and MS1, before we terminate our simulations at $t - t_{\rm merger} \sim 150$ ms.

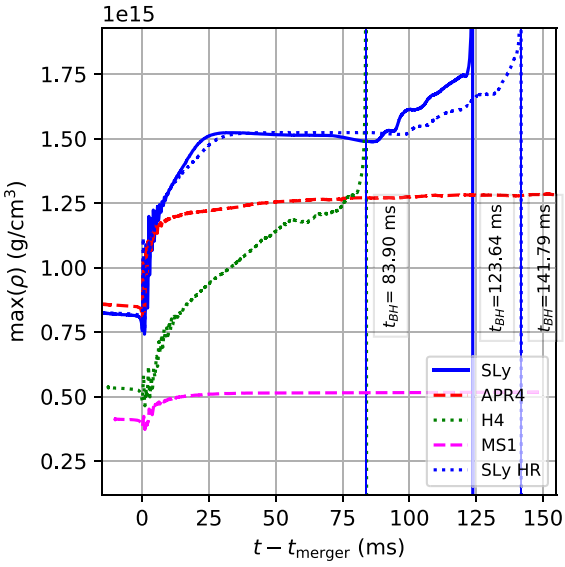

FIG. 1. Maximum density as a function of time for the simulations of the models with the four different EOS (notice that HR is a high-resolution run with the SLy EOS).

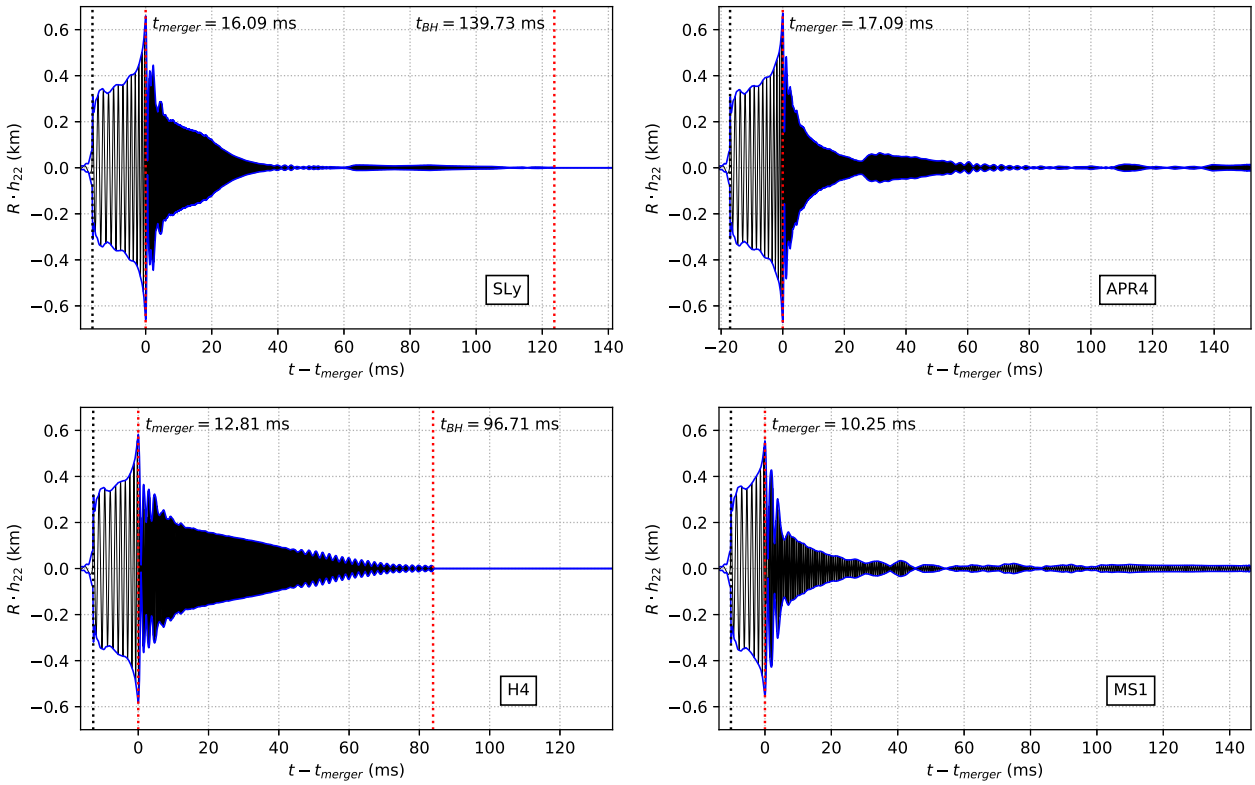

FIG. 2. Scaled h_{22} component of the GW waveform for the four models. The red dotted lines marks the merger time, t_{merger}, and the time of the formation of the black hole, t_{BH}.

The GW signal obtained from the simulations of these four models is presented in Fig. 2. We show the h_{22} component of the GW amplitude (multiplied by the assumed distance to the source, R) (black line) and the absolute value of h_{22} (blue line), assuming an ideal source orientation. The time of merging and the time of the collapse to a black hole are indicated by vertical, dotted red lines. For details on the numerical extraction of the GW signal see [63,69,83].

The evolution of the GW amplitude for the SLy EOS model in Fig. 2 shows a relatively slow decay up to about 20 ms after merger (in this phase, the decay is due to both nonlinear hydrodynamical interactions and GW emission), followed by a second phase of somewhat faster decay, which lasts up to about 65 ms after merger, when the GW emission almost ceases and the remnant has become nearly axisymmetric. However, at about 65 ms after merger, there is a clear revival of GW emission (see [32] and the following sections, for an interpretation of this observation in terms of the excitation of inertial modes by convective instabilities in the remnant).

For the model with EOS MS1, we observe an initial decay of GW emission up to about 40 ms after merger, followed by several episodes of revival of GW emission, up to about 100 ms after merger. At even later times, the remnant radiates GWs at practically a single frequency and at a practically constant amplitude. Such a behavior is expected in the case of a specific, unstable mode saturating at a maximum amplitude, due to a balance between energy gained (by an instability) and energy lost (e.g., by GW emission).

For the model with EOS H4, Fig. 2 reveals an almost linear decay of the GW amplitude for the most part of the time period up to almost 80 ms (shortly after, the remnant collapses to a black hole). However, after 45 ms from merger, a modulation appears in the amplitude evolution, indicating the presence of a second frequency, close to the dominant postmerger frequency (in [32] and the following sections, we give the same interpretation to this second frequency, as in the case of the late-time behavior of the SLy EOS model).

A similar late-time revival (more than 60 ms after merger) of GW emission can be observed for the model with the APR4 EOS. In addition, for this model we observe a strong revival of GW emission already at 25 ms after merger. We will comment on this finding in Sec. III F.

B. Spectrum evolution and Prony's analysis

The general dynamics of the evolution of our four BNS systems can be neatly captured in the time-frequency plots of the h_{22} component of the spherical harmonic decomposition of the GW signal shown in Fig. 3. On top of each spectrogram we also superimpose with thick gray lines the

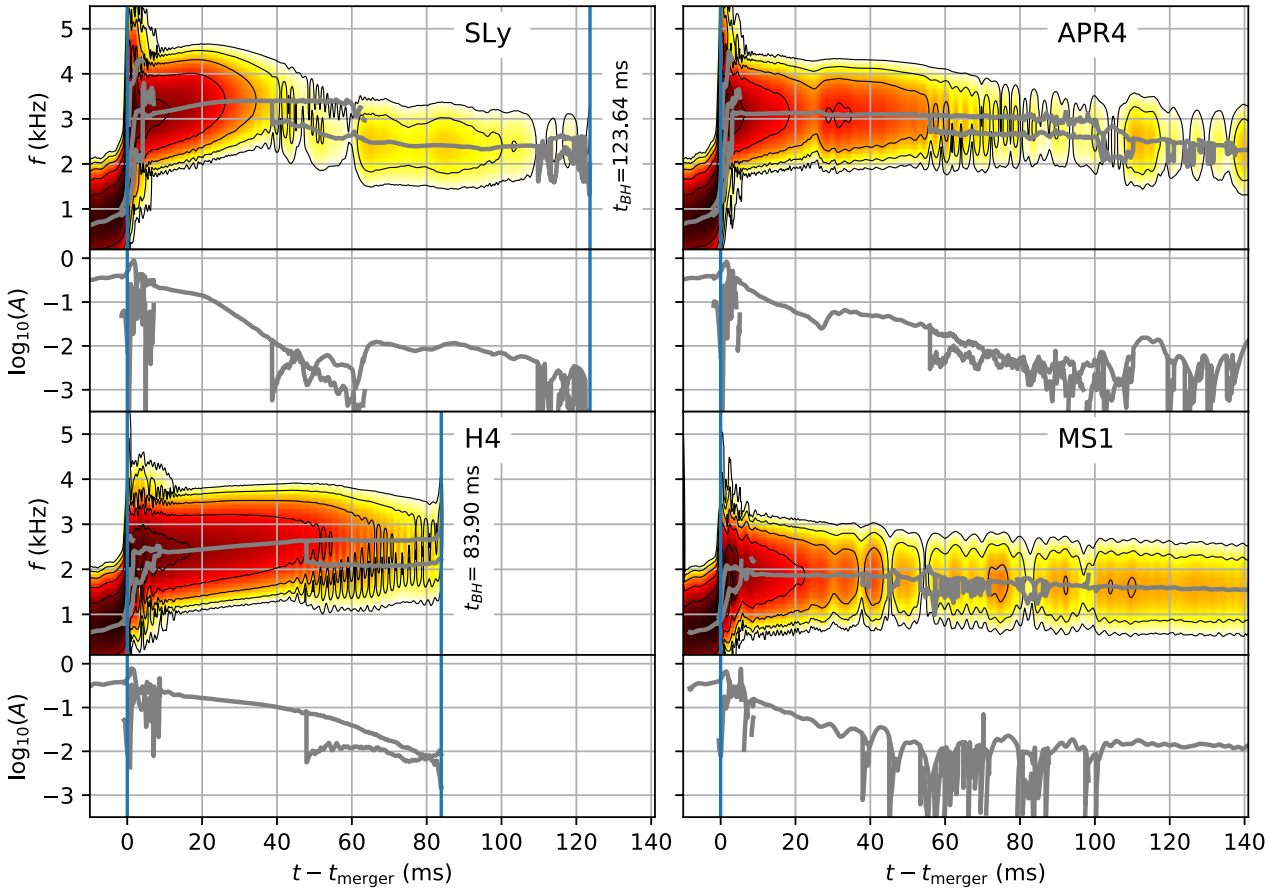

FIG. 3. The top half of each panel shows time-frequency spectrograms of the $l = m = 2$ component of the GW strain for all models. Thick gray lines indicate the frequency of the active modes that mainly responsible for the GW emission at different times. Colors indicate the relative intensity of the spectral density (darker areas correspond to higher intensity). The bottom half of each panel displays the amplitude of the main active modes (in arbitrary units). For the two models that collapse to a black hole within the simulated timescale, the time of black hole formation is reported with respect to the merger time and indicated by the rightmost vertical lines.

time evolution of the frequency of the main active spectral modes of the remnant. This is determined using the ESPRIT Prony's method (employing a moving window interval of 3 ms) as discussed in [63]. The corresponding extracted amplitudes of the modes are also reported in the lower half of each panel in arbitrary units. The leftmost vertical line in each panel of Fig. 3 indicates the time of merger and the rightmost vertical line (for EOS SLy and H4 only) indicates the time of black hole formation.

For the H4 EOS and the SLy EOS, the postmerger remnant survives for over 80 ms and 120 ms, respectively, before collapsing to a black hole. For the MS1 EOS and APR4 EOS, the remnant has not collapsed even after 140 ms. The findings about the mode dynamics presented in [32] continue being valid when adding the H4 and MS1 EOS to the sample. For all four EOS the dominant mode in the early postmerger phase is the $m = 2$ f-mode, with a frequency above 3 kHz for SLy and APR4, about 2.5 kHz for H4, and below 2 kHz for MS1. In all four cases, the evolution of this mode is characterized by a decaying amplitude. As first found by [32], distinct, lower-frequency modes appear later in the evolution, at $t - t_{\rm merger} \sim 35$ ms for SLy and MS1, ~45 ms for H4, and ~55 ms for APR4. This new type of GW emission dominates over the initial $m = 2$ f-mode at late times.

A closer look at our Prony's analysis of the behavior of the postmerger signal for each EOS reveals the following (all times are with respect to the time of merger):

TABLE I. Main properties of the four equal-mass BNS systems studied in this work. The columns report the baryonic mass, M_0, the gravitational mass, M, and the compactness $C \coloneqq M/R$ of the individual stars, the total ADM mass, $M_{\rm ADM}$, the angular momentum, $J_{\rm ADM}$, and the angular velocity of the binary system, Ω_0, at the start of the simulation. All systems have roughly the same initial separation of 44.3 km.

EOS	M_0	M	C	$M_{\rm ADM}$	$J_{\rm ADM}$	Ω_0 (krad/s)
SLy	1.40	1.2810	0.161	2.538	6.623	1.770
APR4	1.40	1.2755	0.166	2.528	6.577	1.767
H4	1.40	1.3004	0.137	2.576	6.802	1.783
MS1	1.40	1.3047	0.129	2.585	6.850	1.787

For the SLy EOS the early postmerger phase (which includes oscillations in the maximum density and transient GW emission of secondary peaks) ends at about 5 ms. After this, the $m = 2$ f-mode is practically the only significant oscillation mode and we observe that its frequency changes secularly with time, at a constant rate of $\sim 1.6 \times 10^{-2}$ kHz/ms up to ∼20 ms. From then on and up to about 60 ms the frequency of the $m = 2$ f-mode remains practically constant. The decay of the amplitude of the $m = 2$ f-mode is slower in the first 20 ms than in the period between 20 ms and 60 ms (at the end of this period this mode has practically faded away). At ∼37 ms an additional mode at a different (lower) frequency appears alongside with the $m = 2$ f-mode. The frequency of the new excited mode is about ∼2.93 kHz. Within about 8 ms from its appearance, the new mode has grown more than an order of magnitude in amplitude and then its amplitude rapidly collapses. Another phase of the excitation, saturation and destruction of a distinct, low-frequency mode (with frequency of roughly 2.7 kHz) follows in the time period between 45 ms and 60 ms. A third such phase lasts between 60 ms and 110 ms, where the dominant mode has a nearly constant frequency of about 2.5 kHz and a nearly constant amplitude (with small variations). Notice that the saturation amplitude of the low-frequency modes in these three periods is similar in order of magnitude. In the following sections (as in [32]) we interpret the low-frequency modes as inertial modes excited by convective instabilities in the remnant (in the model with the SLy EOS we thus observe three such episodes of inertial mode excitation, with somewhat different frequencies, but comparable saturation amplitude—whether it is the same or different inertial modes that are excited in each episode remains to be determined by a detailed mode analysis). At ∼110 ms it is not possible to recognize any mode clearly and at ∼123.6 ms a black hole is formed.

For the APR4 EOS the early postmerger phase ends at about 3.2 ms. At this point there is only one mode with frequency ∼3.1 kHz which remains practically constant up to ∼25 ms. The exponential damping timescale is constant in this time interval. At ∼25 ms there is a small glitch in the frequency of the main mode, which otherwise continues practically constant up to ∼54 ms. Notice that at ∼25 ms the amplitude of the mode increases appreciably on a dynamical timescale, before the damping continues (we will comment on this finding in Sec. III F). The frequency of the main mode continues to be visible up to ∼100 ms, having a somewhat larger damping rate. However, at ∼54 ms an additional mode appears, with a lower frequency of ∼2.70 kHz. Whereas its frequency remains practically constant up to ∼100 ms, its amplitude shows rapid variations, which can be interpreted as several episodes of excitation-saturation-destruction of an unstable mode. Between ∼105 ms and ∼120 ms another such episode takes place (at the same frequency), but this time the saturation amplitude rises higher and remains constant for a longer time. After ∼120 ms a few more episodes are visible at a frequency slightly smaller than in the previous time period. Notice that between ∼98 ms and ∼105 ms another mode with smaller frequency of ∼2 kHz appears in the spectrogram, but with very small amplitude (we cannot exclude that this could be an artifact of the Prony's method).

For the H4 EOS the early postmerger phase ends at ∼6.7 ms when only one mode is present. This mode has an initial frequency of ∼2.37 kHz and changes constantly with a rate of $\sim 7.1 \times 10^{-3}$ kHz/ms up to ∼46 ms after the merger, after which it remains practically constant at ∼2.64 kHz. The exponential damping timescale is constant in this time interval (and becomes somewhat shorter after that). At ∼46 ms a second mode appears at a practically constant, lower frequency of ∼2.11 kHz. This new modes rises in amplitude on a dynamical timescale, saturates quickly and stays at a nearly constant amplitude until black hole formation at ∼84 ms.

For the MS1 EOS the early postmerger phase ends at ∼6.7 ms, when only one single mode is active, with an initial frequency of ∼1.88 kHz that stays practically constant up to ∼35 ms. The exponential damping timescale is constant in this time interval. From ∼35 ms to ∼100 ms one can observe several episodes of the excitation-saturation-destruction of another, lower-frequency mode. As time goes on, the frequency of this second mode decreases. The final episode takes place at ∼100 ms, after which the lower-frequency mode maintains a nearly constant (but slightly decreasing) frequency of ∼1.55 kHz and a nearly constant saturation amplitude.

To summarize, for all four models the postmerger phase can be subdivided into three distinct periods:

(i) *Early postmerger phase* ($0 < t - t_{\rm merger} \lesssim$ 3–7 ms): the main $m = 2$ f-mode frequency and the subdominant frequencies f_{2-0} and/or $f_{\rm spiral}$ are active.

(ii) *Intermediate postmerger phase* (3–7 ms $\lesssim t - t_{\rm merger} \lesssim$ 35–50 ms): only the $m = 2$ f-mode is active.

(iii) *Late postmerger phase* ($t - t_{\rm merger} \gtrsim$ 35–50 ms): low-frequency modes appear in several episodes of excitation-saturation-destruction.

In addition, we notice a sudden revival of the $m = 2$ f-mode in the intermediate phase (see discussion in Sec. III F).

In the following sections, as in [32], we will identify the low-frequency modes in the late postmerger phase as inertial modes, driven by convective instabilities.

C. Spectral content in the different stage of the dynamics

According to the temporal subdivisions discussed in the previous section, it is meaningful to single out the particular contributions of different time windows in the GW spectra for each of the EOS. The corresponding spectra are

displayed in Fig. 4. This figure shows the scaled PSD $2\tilde{h}\sqrt{f}$ of the GW signal for a maximally aligned source at a distance of 50 Mpc (where $\tilde{h}$ is the Fourier transform of the GW signal). From top to bottom each row corresponds to the spectra of the models with the SLy, APR4, H4, and MS1 EOS, respectively. The thin-dashed-black lines in all of the panels display the entire spectra computed taking into account the complete temporal evolution of the simulations, i.e., $t - t_{\rm merger} \in [-20, 140]$ ms. On the other hand, the colored thick-solid lines indicate the corresponding spectra for the particular time window reported in the top of each frame. To obtain a cleaner separation of the contributions to the spectra due to the various time intervals considered, we do not apply any windowing functions. As a result, the FFT includes small artifacts due to the finite size of the time intervals. As the time window changes from left to right, the more prominent features in the spectra can be seen to readjust accordingly.

The vertical red dashed lines in the first column (roughly corresponding to the early postmerger phase) of Fig. 4 mark

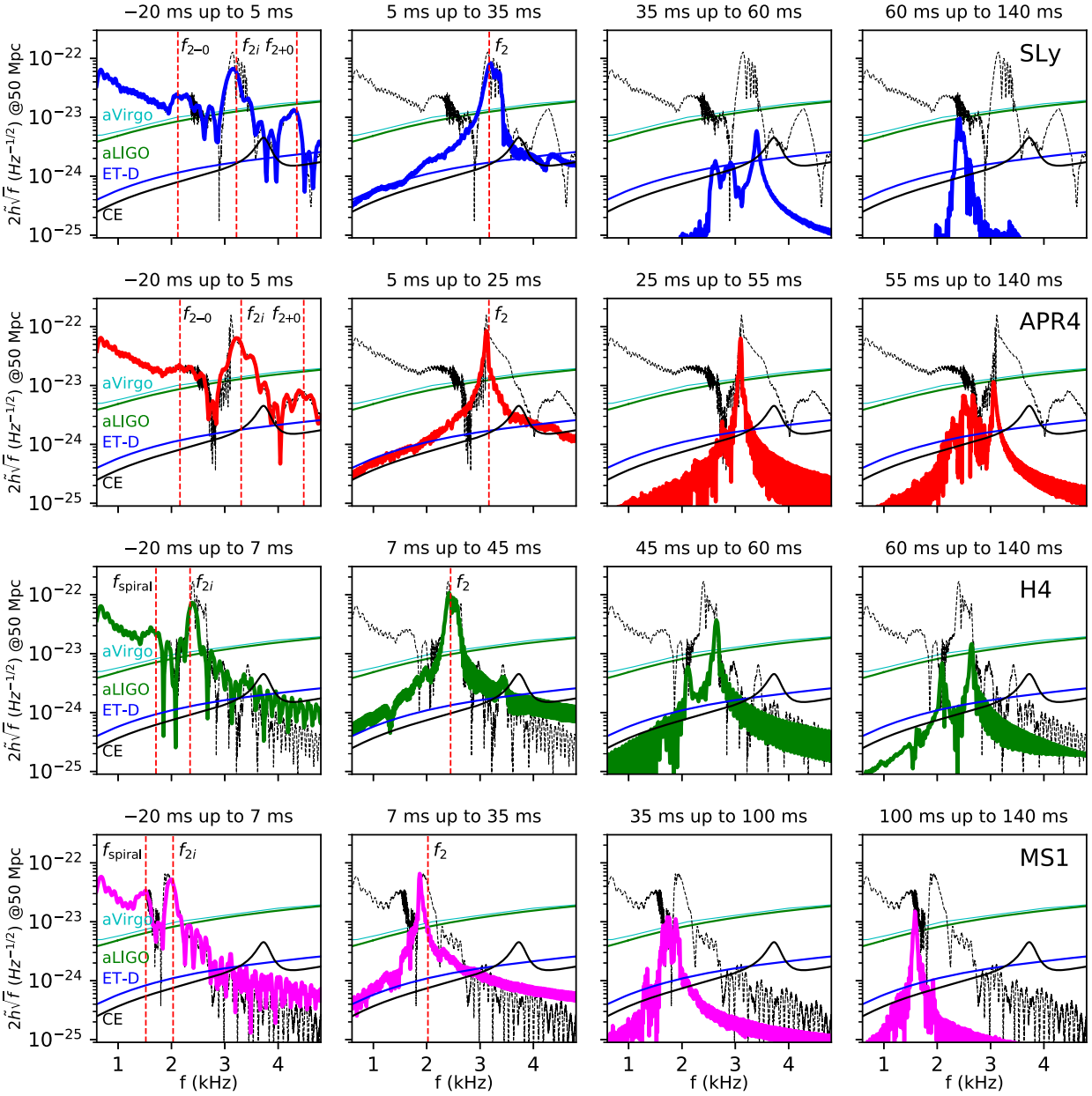

FIG. 4. GW spectra for a BNS merger at 50 Mpc with optimal orientation (one row for each EOS model). The spectra are shown for the entire GW signal (thin-dashed lines) and for different restricted time windows (indicated at the top of each frame) in order to emphasize the contribution of the dominant spectral components at different times. The design sensitivities of Advanced Virgo [99], Advanced LIGO [100], Einstein Telescope [101], and Cosmic Explorer [102] are shown for reference.

the position of the initial frequency f_{2i} of the dominant $m = 2$ f-mode and of the subdominant peaks f_{2-0}, f_{2+0} (for the models with EOS SLy and APR4) and $f_{\rm spiral}$ (for the models with EOS H4 and MS1). These peaks can be obtained directly from the GW spectrum, but also using the ESPRIT Prony algorithm. Our identification of the subdominant peaks is in agreement with the spectral classification of the postmerger GW emission in [24], see also [17]. Notice that in other works, the f_{2-0} and $f_{\rm spiral}$ peaks have been named, collectively, f_1 and the f_{2+0} peak has been named f_3.

In the second column (roughly corresponding to the intermediate postmerger phase) of Fig. 4, the vertical red dashed lines mark the position of the f_2 frequency peaks of the dominant $m = 2$ f-mode (notice that f_2 can remain very close to its initial value f_{2i}, or it can display a secular time variation).

For all models, the spectra corresponding to the entire duration of the simulations is clearly dominated by the $m = 2$ f-mode (f_2) in the EOS-dependent frequency range ~2–3.5 kHz. On the other hand, when selecting the signal in the different time periods displayed in Fig. 4 the dominant peaks in the spectra begin to change. In the final time interval, $t - t_{\rm merger} \in [60, 140]$ ms, the spectrum is dominated by a peak at frequency ~2.38 kHz in the case of the SLy EOS and well below 2 kHz for the MS1 EOS. Moreover, in the case of the APR4 EOS there are several nearby lower-frequency peaks contributing to the GW spectrum in the late postmerger phase.

In the intermediate postmerger phase, the spectra for the EOS SLy model (5 ms to 35 ms) and the EOS H4 model (7 ms to 45 ms) are consistent with the Prony's method results that, for these models in these time periods, the dominant f_2 frequency is subject to a slow drift to higher frequencies. This is due to the fact that in this time period the remnant experiences an almost steady drift to higher maximum densities (see Fig. 1). It is well known that the frequency of the fundamental fluid modes of a star scale as the square root of the average density (see e.g., [103]). Notice that the remnants for these two models have a mass relatively close to the threshold mass for collapse to a black hole (and indeed they do collapse within the duration of our simulations). The panels in Figure 4 also show the design sensitivities of Advanced Virgo [99] and Advanced LIGO [100] as well as those of third-generation detectors Einstein Telescope [101] and Cosmic Explorer [102]. In [32] we discussed the prospects of detectability of the low-frequency modes excited at sufficiently long times after merger for models SLy and APR4. In the current work our simulations account for additional models with the H4 and MS1 EOS. In all cases we find that there is sufficient power in the lower-frequency modes to render them potentially observable by third-generation detectors. For a source at 50 Mpc, the expected Cosmic Explorer [102] S/N ratios for optimal use of matched filtering techniques for the signal emitted in the time intervals used in the last two columns of Fig. 4 are ~1.3 and ~3.5 for SLy, ~9.1 and ~3.7 for APR4, ~11.6 and ~5.1 for H4, ~9.7 and ~8.3 for MS1 EOS, respectively (for the Einstein Telescope-D [101] they are ~1.2 and ~2.5, ~8.0 and ~2.9, ~8.7 and ~3.7, ~6.4 and ~5.5, but enhancement can be expected due to the triangular arrangement with three nonaligned interferometers). We note that the S/N ratio is significantly higher in the first ~40 ms after merger for each model, while it becomes almost two orders of magnitude smaller when the inertial modes appear and the signal can only be observed by the next generation detectors, as mentioned above.

D. Mode eigenfunctions

To analyze and show the difference of the various oscillation modes we have performed the FFT transform in time segments of 5 ms of the density distribution and extracted the Fourier amplitude at selected fixed frequencies (this correlates with the eigenfunction of a given mode, as shown in [21,104]). For each segment we assign the central time as a label. In Figs. 5–9 we summarize the behavior of the density eigenfunction of each model for the frequencies we mentioned in Sec. III B at different times. Each panel of those figures is normalized to the maximum value of the density eigenfunction shown. The first column of each figure shows the eigenfunction of the dominant $m = 2$ f-mode for each model in both the equatorial (XY) and the vertical (XZ) planes. In the equatorial plane there are no nodal lines, indicating that this is a fundamental mode.

The APR4 EOS shows an excited mode already after ~30 ms in the postmerger phase, which is not visible in the spectrogram of Fig. 3 produced using the Prony's method, but is clearly visible from the density eigenfunction profiles

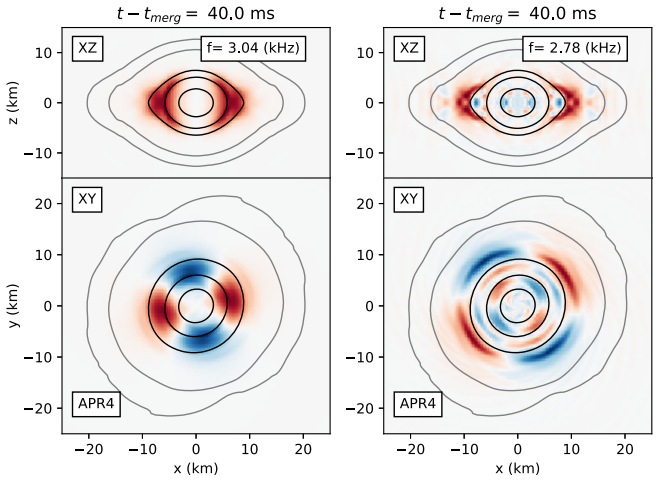

FIG. 5. Density eigenfunctions in the vertical and equatorial plane of the APR4 model at 40 ms after merger. The black and gray lines are isocontours of the rest-mass density. The left column displays the $m = 2$ f-mode and the right column corresponds to an inertial mode in the late postmerger phase.

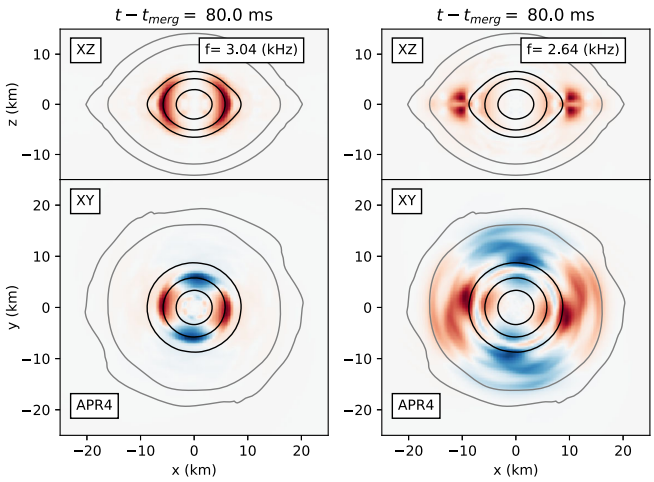

FIG. 6. As in Figure 5, but at 80 ms after merger.

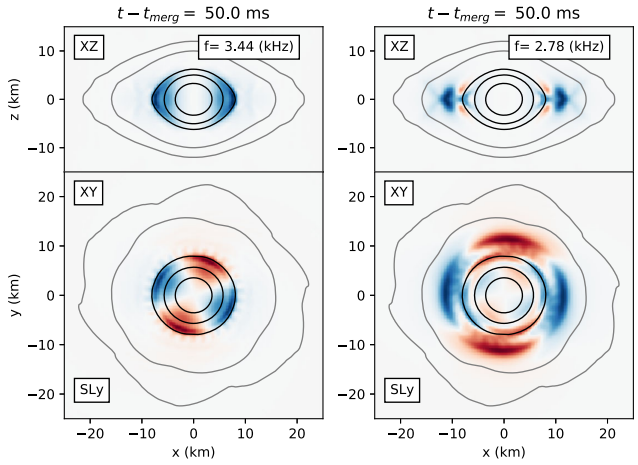

FIG. 7. As in Fig. 5, but for EOS SLy at 50 ms after merger.

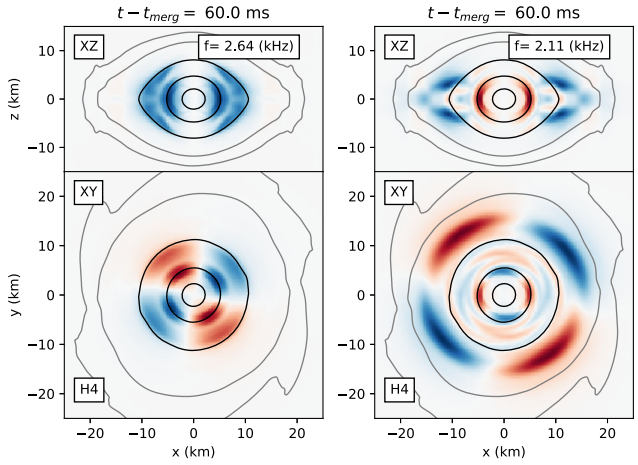

FIG. 8. As in Fig. 5, but for EOS H4 at 60 ms after merger.

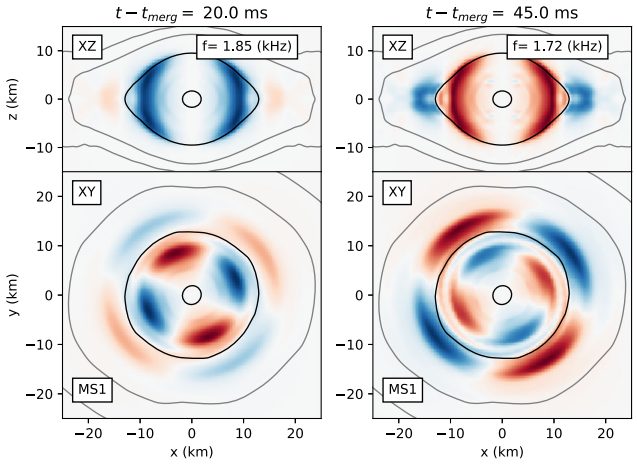

FIG. 9. As in Fig. 5, but for EOS MS1 at 20 ms and 45 ms after merger.

in Fig. 5. This is due to the fact that this excited mode is extremely weak and cannot be distinguished using the Prony's method. In Fig. 9 we note that the $m = 2$ f-mode for the MS1 does show a nodal line far from the center, in the extended, low-density envelope. This behavior is not surprising for differentially rotating stars in rapid rotation, where the rotational forces can modify the structure of the eigenfuction in the low-density regions near the surface, see, e.g., [104].

The SLy EOS presents only an $m = 2$ f-mode until ∼35 ms after the merger, where we note the appearance of an excited mode at lower frequency. The main mode is then suppressed and only the excited one will survive until the remnant forms a black hole in the late postmerger phase. For the H4 EOS we note that the main $m = 2$ f-mode is the only mode present until ∼45 ms when the excited mode at lower frequency appears. The two modes then survive ∼30 ms until the HMNS collapses to a black hole.

The excited low-frequency modes in the late postmerger phase have the characteristics of inertial modes. Their frequency is in the right range, with the dominant mode always having a frequency somewhat smaller than the maximum rotational frequency in the star (although our sample of models is small, it appears that the frequency of the dominant mode in the late postmerger phase correlates with the rotational frequency of the star, as expected from inertial modes). Their eigenfunction has a peak in the low-density outer parts of the stars, having more nodal lines than the fundamental quadrupole mode. We note that inertial modes in rapidly rotating stars can be axial-led (reducing to axial r-modes in the slow-rotation limit) or polar-led (reducing to g-modes in the slow-rotation limit) [105,106]. The latter are also called gravitoinertial modes. A precise identification of the character of the excited modes would require a detailed comparison with linear oscillations of quasiequilibrium models. Because the inertial modes observed in the postmerger phase are excited by

convective instabilities in the outer layers of the remnant, it is likely that at least some (or most) of the inertial modes we observe are polar-led, i.e., gravitoinertial modes (but the presence of axial-led inertial modes cannot be excluded without further detailed study).

E. Convective instability and inertial modes

The appearance of lower-frequency modes in the late stage of our simulations can be interpreted as inertial modes, for which the Coriolis force is the dominant restoring force. The growth of such modes is caused by a convective instability that appears in the nonisentropic remnant just before the excited modes start to grow from a small amplitude.

As we note in [32], the local convective stability depends on the Schwarzschild discriminant, which is defined as

$$A_\alpha = \frac{1}{\varepsilon + p}\nabla_\alpha \varepsilon - \frac{1}{\Gamma_1 p}\nabla_\alpha p, \tag{1}$$

where

$$\Gamma_1 := \frac{\varepsilon + p}{p}\left(\frac{dp}{d\varepsilon}\right)_s = \left(\frac{d\ln p}{d\ln \rho}\right)_s \tag{2}$$

is the adiabatic index around a pseudobarotropic equilibrium and where ε is the energy density. Regions where $A_\alpha < 0$ are convectively stable, while regions where $A_\alpha > 0$ are convectively *unstable*. Since in this work we are using a piecewise polytropic approximation for the construction of our models, we calculate Γ_1 as

$$\Gamma_1 = \Gamma_{\rm th} + (\Gamma_i - \Gamma_{\rm th})\frac{K_i \rho^{\Gamma_i}}{p} \tag{3}$$

where K_i and Γ_i are the polytropic constant and exponent in the ith piece of the EOS, respectively, and $\Gamma_{\rm th}$ is the adiabatic index added for the thermal treatment (see Appendix C for further details). In order to determine the convective stability in the long-living remnant, we calculate A_r and A_θ in the equatorial and vertical planes at different times.

The results of the computation of the Schwarzschild discriminant in the equatorial plane for each model considered in this work are displayed in Fig. 10 at selected evolution times. In this figure convectively unstable regions ($A_r > 0$) are represented using a dark color. The first row of Fig. 10 shows the case of the SLy EOS and we note that the remnant is stable in the first ∼35 ms of the postmerger phase and the GW spectrum is dominated by the $m = 2$ f-mode. After ∼39 ms we observe the formation of a convectively unstable ring, which corresponds to the outer layer of the hot ring which is visible in the second panel of the third row of Fig. 11, depicting temperature isocontours. This coincides with the first appearance of inertial modes. At ∼65 ms the convectively unstable ring has expanded to the lower density regions of the remnant and appears fragmented, which correspond to the strong growth of an inertial mode at 2.38 kHz. The amplitude of the mode remains almost constant throughout the following phase, while the convectively unstable regions keep expanding in the envelope until the remnant finally collapses to a black hole.

In the second row of Fig. 10 we display the Schwarzschild discriminant for the H4 EOS, which presents a slightly different situation compared to the SLy EOS. Around ∼32 ms we note that there are unstable regions in the outer layer of the core which are due to the presence of hot spots (not shown in this work) generated by the shock heating produced during the merger. At ∼45 ms an unstable ring appears just outside the core, corresponding to the growth of an inertial mode with frequency 2.11 kHz. The unstable regions expand and become fragmented at a later time whereas the amplitude of the inertial mode continues to grow until the remnant collapses to a black hole after ∼84 ms.

The evolution of the Schwarzschild discriminant for the model with the APR4 EOS, which is shown in the third row of Fig. 10, appears at first glance to be similar to that of the SLy EOS. However, it does show a crucial difference, visible in the first panel of the figure. This panel displays a generally stable remnant despite, as we have already observed in Sec. III D, the presence of an additional excited mode by this evolution time (∼35 ms). The appearance of this mode is not triggered by the expansion of the convectively unstable region, since in this phase the remnant has a corotating region which is visible in Fig. 13. This figure shows that the mode frequency is lower than the peak of the rotational profile at $t = 25$ ms, which corresponds to the maximum rotation frequency for the APR4 EOS model. As in the case of the SLy EOS, a convectively unstable ring forms at a later time, a few milliseconds before the appearance of inertial modes. The unstable regions starts expanding in the lower density regions of the remnant, leading to the growth in amplitude of such modes.

Finally, in the case of the MS1 EOS, the different snapshots in the last row of Fig. 10 show convectively unstable regions fairly spread over the entire postmerger remnant from earlier times than for the other three models. Notice that for this EOS, the episodes of excitation-saturation-destruction of a lower-frequency inertial mode already start at earlier times than shown in Fig. 10.

Figure 11 shows snapshots of the density and temperature in the equatorial plane for the model with the SLy EOS, at different times relative to the time of merger. In the first two rows of the figure we display the density and temperature profiles of the postmerger remnant, up to a time of 29 ms, when the $m = 2$ f-mode is still dominant. We note that in this phase there are two hot spots where the remnant is deformed and which start to diffuse. This is the

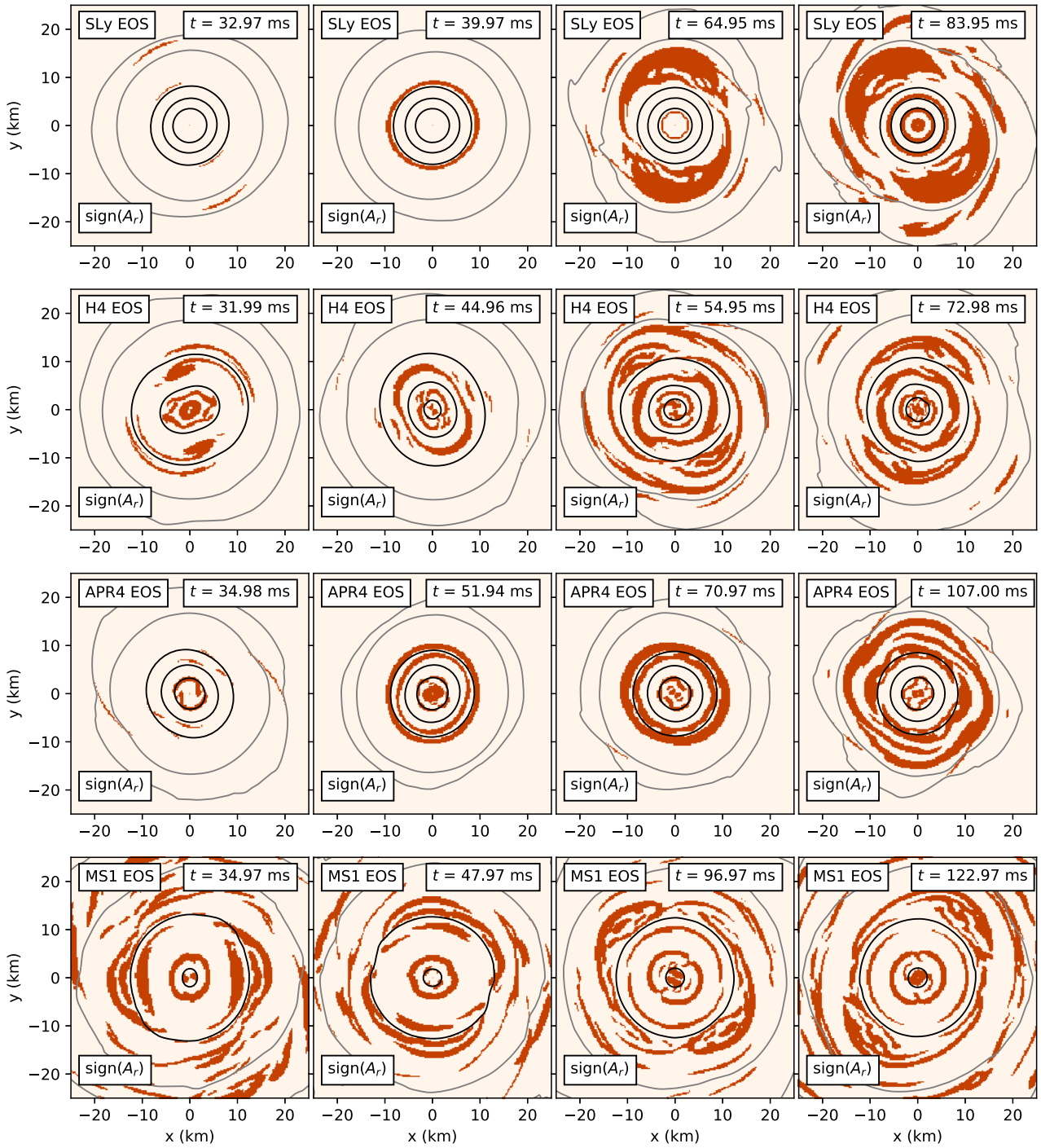

FIG. 10. Snapshots of A_r in the equatorial plane. Each row corresponds to a different EOS model and each column to different times after merger. Dark color indicates regions where $A_r > 0$, which corresponds to convective instability (see text for details).

expected behavior, as found in simulations with many different numerical codes (see, e.g., [18] and references therein). In the last row of the figure we show snapshots of only the temperature at times between 33 ms and 84 ms. A hot shell forms around the cold core at ∼33 ms. Later, at around 65 ms, a second hot ring is forming in the equatorial plane and by 84 ms the temperature of the inner shell has risen visibly, reaching about $T \sim 50$ MeV.

In our simulations, convection is exciting specific, global inertial modes. This is not unexpected, see, e.g., [107–110]. We note that the inertial modes are excited when the temperature profile in the remnant has become nearly

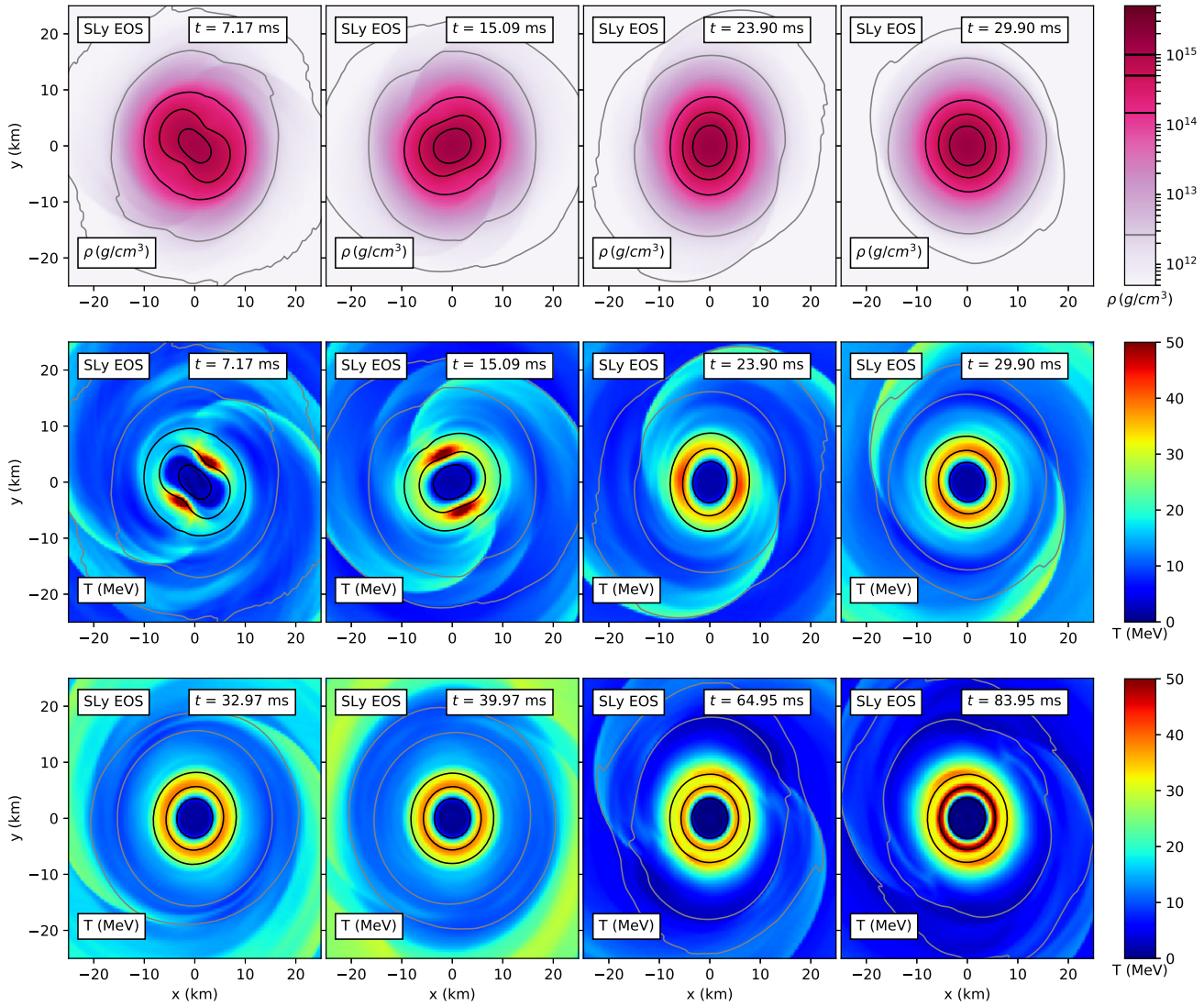

FIG. 11. Snapshots of the density and temperature in the equatorial plane for the model with the SLy EOS at different times relative to the time of merger (see text for details).

axisymmetric (by that time, the amplitude of the peak $m = 2$ f-mode oscillation has diminished). In contrast, the initial strongly nonaxisymmetric temperature pattern (essentially in the form of two hot spots) does not seem to lead to the excitation of global modes. This is true for all four models considered: inertial modes start growing once the temperature distribution has become sufficiently circular in the equatorial plane.

We stress that the convective instability found in our simulations is solely triggered by the thermal gradient created by shock heating at the time of merger. Hence, in our setup no additional physics (e.g., radiative cooling) is necessary to create a thermal gradient. As shown in Fig. 11, for $t > 30$ ms after merger, the core of the remnant is cold and is surrounded by a shell of hot matter, with the temperature reaching a peak at about 5 km from the center. Beyond that distance, the temperature decreases steeply with radius and it is this thermal gradient that is responsible for triggering the convective instability. A similar situation has been recently reported by [44] who study rotating stars with nonbarotropic thermal profiles. This work shows that convection sets in without requiring additional physics, as long as there is a negative entropy gradient when the density is below a critical density (see Eq. (C7) in [44]), which is the case in our simulations.

In particular, numerical dissipation does not play a role in triggering the convective instability. It can only dampen the instability, once it sets in, or entirely prevent it, if it is too strong. In our simulations, the numerical dissipation is sufficiently small to allow for the instability to grow and saturate. Figure 16 in Appendix A displays the evolution of different norms of the Hamiltonian constraint violations, at three different resolutions (for EOS Sly as a representative case). The violations converge with resolution and remain sufficiently small throughout the duration of the simulation.

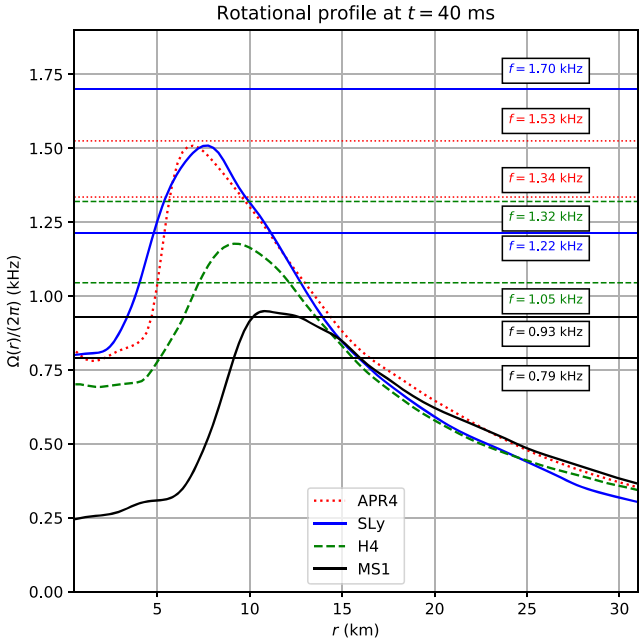

FIG. 12. Rotational profiles $\Omega/2\pi$ vs coordinate radius r, for the four different EOS models at $t = 40$ ms after merger. The horizontal lines indicate the pattern speed frequencies of the two main $m = 2$ modes for each model. The colors of the horizontal lines are the same as for the EOS labels.

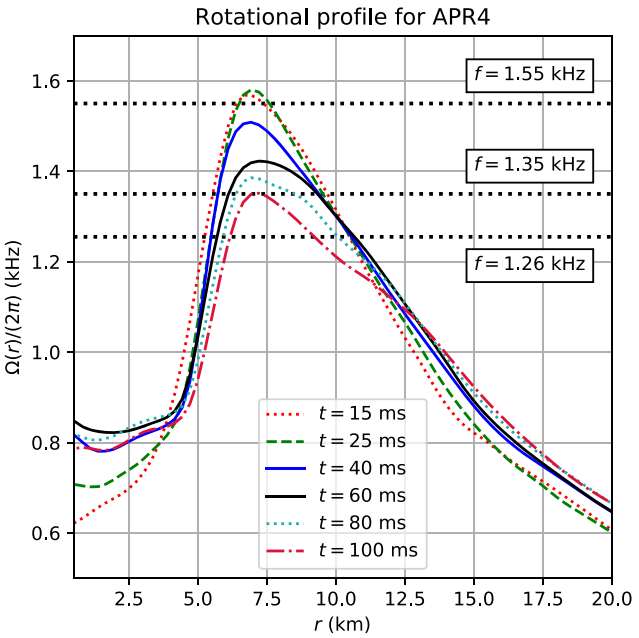

FIG. 13. Rotational profiles $\Omega/2\pi$ vs coordinate radius r, for the model with EOS APR4 models at different times after merger. The horizontal lines indicate the pattern speed (assuming $m = 2$) of the f-mode (1.55 kHz) and of the main inertial mode at the start (1.35 kHz) and the at end (1.26 kHz) of the convectively unstable phase.

F. Corotation and mode revival

As noted in the introduction, the state of the system in the postmerger phase is a single (excited) differentially rotating neutron star with a nontrivial rotational profile, which is shown in Figs. 12 and 13. Moreover, there is also a nontrivial temperature profile (and indeed a nontrivial entropy) profile, in which the temperature has an off-center maximum (a circle in the equatorial plane at late times). The rotational and thermal structure of the postmerger remnants in our simulations is in agrement with results in the literature (see, e.g., [70,73,111]) where similar assumptions were made (only when assuming a very strong physical viscosity different profiles are found, see [75]). The remnant may be subject to various instabilities, namely the dynamical bar-mode instability (see [112–114] and references therein), the secular Chandrasekhar–Friedman–Schutz (CFS) instability [39,40] and shear instabilities that can develop in differentially rotating stars (see, e.g., [43] and references therein). In addition, our results reveal the possibility of the excitation of additional modes in the postmerger phase for sufficiently long times. We discuss next how the frequency of the excited inertial mode is related to the rotational profile of the neutron star at the late stage of the postmerger dynamics.

In Fig. 12 we show the rotational profile (angular velocity vs distance in the equatorial plane) of the four models at 40 ms after merger, along with the pattern speed frequency for the two main modes in each model, indicated by the horizontal lines. For $m = 2$ modes the pattern speed frequency is half of the associated GW frequency. We note that at this stage of the evolution only the APR4 and MS1 models are still in corotation with the mode pattern speed.

In Fig. 13, we focus on the model with the APR4 EOS and show the rotational profile at different times, along with the pattern speed of the $m = 2$ f-mode (1.55 kHz) and of the main inertial mode at the start of its excitation (1.35 kHz) and at the end of the simulation (1.26 kHz). It is interesting to notice that the revival of the amplitude of the $m = 2$ f-mode at 25 ms after merger coincides with the mode being in corotation with the HMNS in a small region. This process is possible when the corotation of the star occurs at the same time as the convective instability of a small region of the star. In this case, as very small regions of the remnant present $A_r > 0$ at 25 ms, angular momentum from the rotation of the star is injected into the main f-mode.

IV. CONCLUSIONS

We have presented the results of new numerical simulations of BNS systems in full general relativity, where the simulations have been extended up to ∼140 ms after merger. In addition to the results for models based on the SLy and APR4 EOS we already discussed in [32], and whose analysis has been significantly extended here, we

have also studied models equipped with two more EOS, namely H4 and MS1 EOS. The main focus of this work has been the analysis of the spectrum of the postmerger GW signal. Our investigation has been driven, in particular, by our aim to provide further evidence in support of our claim in [32] about the potential existence of new families of oscillation modes excited in long-lived postmerger remnants (in addition to the main fluid quadrupole f-mode) at sufficiently late times of the evolution.

In [32] we already observed that the appearance of convectively unstable regions and the excitation of inertial modes in remnants that survive for a long time after merger depend on the rotational and thermal state of the remnant and affect the HMNS dynamical evolution. In all further cases investigated in the present work, the late-time excitation of inertial modes to large amplitudes has been corroborated. Indeed, inertial modes become the dominant modes for the GW emission in the postmerger phase of pulsating HMNS for times from about 40 ms up to at least 100 ms after merger. We have found that the postmerger phase can be subdivided into three phases: an early postmerger phase (where the quadrupole mode and a few subdominant features are active), the intermediate postmerger phase (where only the quadrupole mode is active) and the late postmerger phase (where convective instabilities trigger inertial modes). For all of the models of our sample, the impact of the inertial modes in the GW spectrum is significant, appearing at signal-to-noise ratios of immediate interest for 3rd-generation detectors, such as the Cosmic Explorer [102] and the Einstein Telescope [101]. This allows for the possibility of probing not only the cold part of the EOS but also its dependence on finite temperature.

Recently [44] have analyzed convectively unstable rotating neutron stars with nonbarotropic thermal profiles (as in the case of binary neutron star remnants) reporting a growth timescale of convection of $\mathcal{O}(10)$ ms close to the center and $\mathcal{O}(0.1)$ ms at lower densities (close to the surface). These timescales are compatible with those presented in [32] and further corroborated in this work. Our study has neglected the effects of shear and bulk viscosity in the star as well as the effective viscosity due to MHD turbulence. In view of our results, it will be important to investigate the influence of viscosity on the lifetime of the remnant and their impact on the rotational profiles of the HMNS, as this might affect the potential excitation of inertial modes. Recent work by [75,76], in which effective shear viscosity was modelled through the so-called viscous α-parameter, has shown that the degree of differential rotation in the postmerger remnant is significantly reduced in the viscous timescale, $\lesssim 5$ ms, for $\alpha \sim \mathcal{O}(10^{-2})$. It remains to be found if such (high) values of the α-parameter are reached in MHD simulations of BNS mergers involving pulsarlike magnetic-field strengths in the inspiral phase.

ACKNOWLEDGMENTS

This project greatly benefited from the availability of public software that enabled us to conduct all simulations, namely "LORENE" and the "Einstein Toolkit". We express our gratitude to everyone that contributed to their development. We have benefited from discussions with Alessandro Drago, Giuseppe Pagliara, Silvia Traversi and Masaru Shibata and we are very grateful to them. We acknowledge PRACE for awarding us access to MARCONI at CINECA, Italy, under Grant No. Pra14_3593. This work also used resources provided by the CINECA-INFN agreement that provides access to GALILEO and MARCONI at CINECA and by the Louisiana Optical Network Initiative (QB2, allocations loni_hyrel, loni_numrel, and loni_cactus), and by the LSU HPC facilities (SuperMuc, allocation hpc_hyrel). J. A. F. acknowledges financial support provided by the Spanish Agencia Estatal de Investigación (Grants No. AYA2015-66899-C2-1-P and No. PGC2018-095984-B-I00), by the Generalitat Valenciana (PROMETEO/2019/071) and by the European Union's Horizon 2020 research and innovation (RISE) programme H2020-MSCA-RISE-2017 Grant No. FunFiCO-777740. F. L. is directly supported by, and this project heavily used infrastructure developed using support from, the National Science Foundation in the USA (Grants No. 1550551, No. 1550461, No. 1550436, No. 1550514). N. S. is supported by the ARIS facility of GRNET in Athens (GWAVES and GRAVASYM allocations)" Support from INFN "Iniziativa Specifica NEUMATT" and by the COST Actions MP1304 ("NewCompStar") and CA16104 ("GWVerse"), is also kindly acknowledged.

APPENDIX A: COMPARING SIMULATIONS AT DIFFERENT RESOLUTIONS

The convergence properties of the numerical code and the accuracy of the simulations were discussed in [69]. Here, we compare the long-term evolution of the model with EOS SLy using three different resolutions of the innermost grid, namely $dx = 369$ m, $dx = 277$ m (the standard resolution in this work), and $dx = 185$ m (which is about five times more computationally expensive). Figure 14 shows the spectrogram and the Prony's analysis for the two highest resolutions, while Fig. 15 shows the comparison of results of the Prony's analysis for all the three considered resolutions. From the data shown in these figures we conclude that the appearance of the convective instabilities, and the associated excitation of inertial modes, happens at somewhat later times as the resolution is increased. Likewise, black hole formation is delayed in all three cases, taking longer times for higher resolutions, as discussed in [69]. Also, there are three (instead of two) episodes of excitation-saturation-destruction before the final excitation of a long-lasting inertial mode with stable

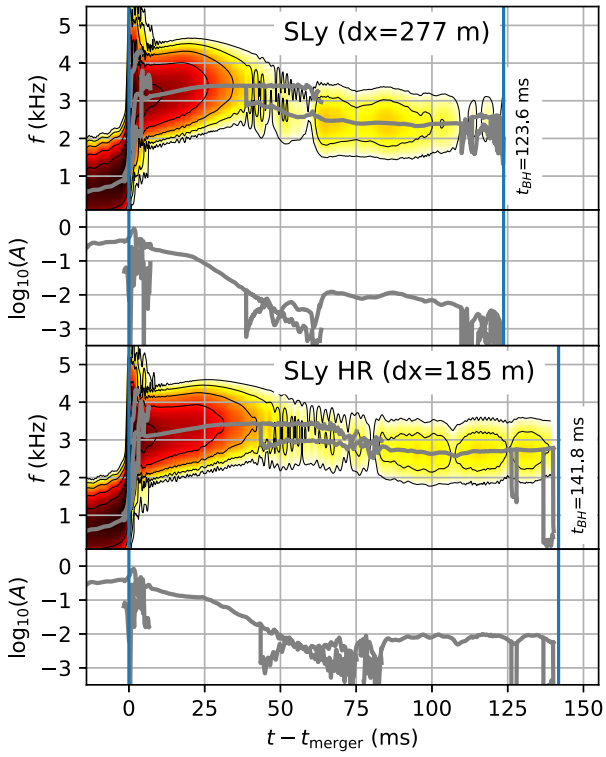

FIG. 14. Time-frequency analysis for the model with EOS SLy at two different resolutions (see text for details).

saturation amplitude. At the lowest resolution, the appearance of an inertial mode (dashed blue line in Fig. 15) is rapidly suppressed due to the collapse of the HMNS to a black hole. For the standard and high-resolution

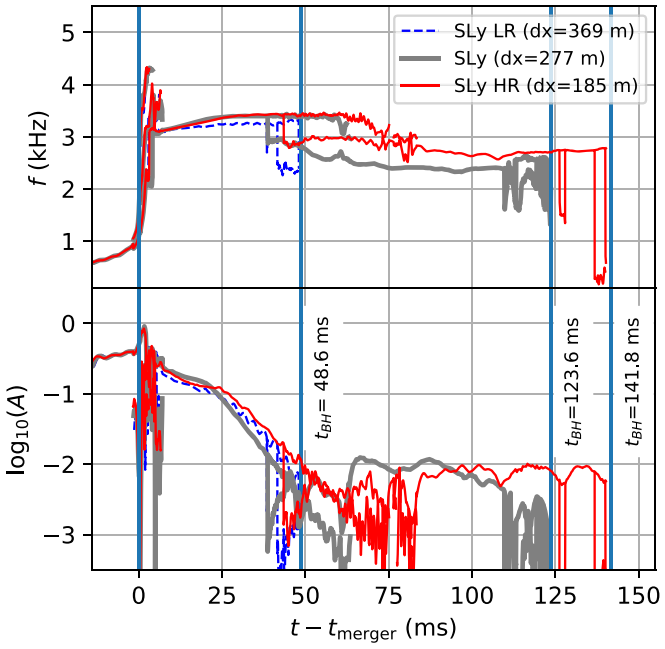

FIG. 15. Comparison of the Prony analysis for the model with EOS SLy at three different resolutions.

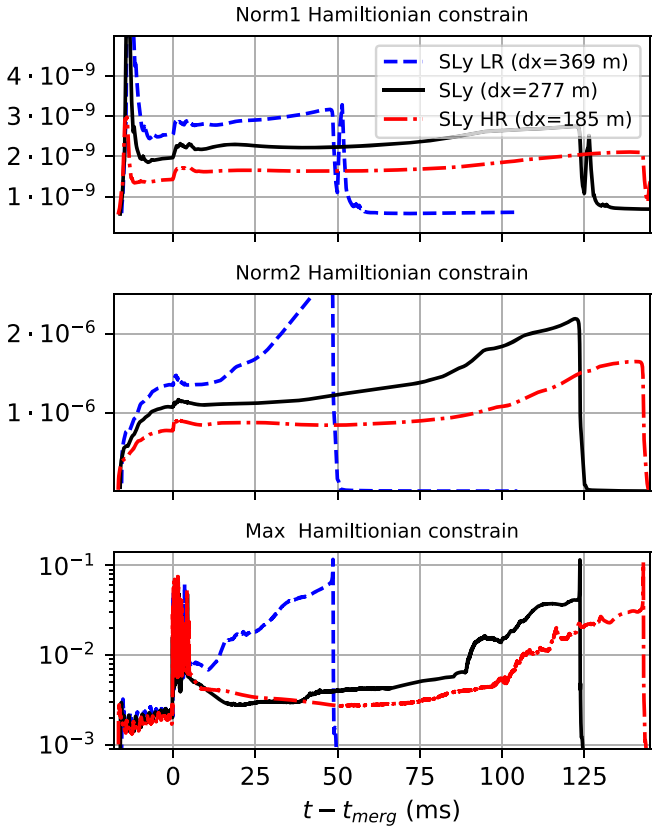

FIG. 16. Hamiltonian constraint violation for different resolutions of the model with EOS SLy.

simulations this mode survives for a longer time due to the smaller numerical dissipation at higher resolutions. For a resolution of $dx = 185$ m the inertial mode appears somewhat later and at a higher frequency than for $dx = 277$ m and $dx = 369$ m since the dissipation at such resolution is smaller and leads to a slightly different hydrodynamical evolution. However, the frequency of the main f-mode does not depend strongly on the resolution.

Whereas we do observe an overall delay in the appearance of various dynamical features in the simulations (which could be due to a better preservation of angular momentum at higher resolution) the qualitative features between the three resolutions remain the same. The results of Fig. 15 seem to contradict the assertion in [115] that some features in the frequency spectrum reported in [32] and also here disappear using higher resolution. We expect that this discrepancy can be resolved by a closer examination of the numerical data in [115], if these become available (or by additional high-resolution simulations). We further comment on this issue in Appendix B.

Figure 16 depicts the violation of the Hamiltonian constraint $\mathcal{H}(x)$ for the simulation of the model with EOS SLy as a representative case and at the same three numerical resolutions. The top panel shows the L_1 norm (i.e., the coordinate integration over the whole grid of $|\mathcal{H}(x)|$), the middle panel depicts the L_2 norm (the

corresponding integration of $|\mathcal{H}(x)|^2$) and the bottom panel shows the maximum of the constraint violation of $\mathcal{H}(x)$ over the whole grid. The average quantities converge when increasing the grid resolution. The same holds true for the maximum value of $\mathcal{H}(x)$ except for the short time in which the two neutron stars merge. The largest constraint violations are attained at black hole formation, as usual in this type of simulations. Overall, this figure shows that the simulations at different resolutions are consistent and that the violations converge with resolution and remain sufficiently small throughout the duration of the simulation.

APPENDIX B: NOTES ON PREVIOUS RESULTS FOR SIMULATIONS LASTING 100 MS AFTER MERGER

Our study is not the first one in which the postmerger phase of a binary neutron star merger is evolved for timescales of about 100 ms. Previous works, all of them fairly recent, include [115–119]. Because of the very small amplitude of the GWs emitted in the late convective phase (as opposed to the large amplitude emitted by hydrodynamical motions during the early phase) one can easily miss the presence of convectively-excited modes in the late postmerger phase, or one can simply dismiss these as artifacts, without further analysis. To the best of our knowledge, other groups have not specifically examined long-term simulations in terms of eigenfunctions or indicators of convective instability. The studies of [116,117] report the results of simulations of binary neutron star mergers with initial data constructed with a simple polytropic $\Gamma = 2$ EOS and evolved as an ideal fluid with $\Gamma_{\rm th} = 2$, extending up to 140ms. Similarly long-lasting simulations for the same EOS are discussed in [118]. None of those investigations report the late-time excitation of inertial modes in the remnant. This indicates that such modes are likely not easily excited when the initial data and the ideal fluid EOS have the same index Γ (notice, e.g., that in [116] that main $l = m = 2$ f-mode still has a large amplitude at the end of the simulation, whereas in our simulations the convective instabilities always set in only after the amplitude of $l = m = 2$ f-mode has diminished).

The work of [119] shows the presence of a second mode at late postmerger times. In the top panel of their Fig. 16 they show the amplitude of the h_{22} GW-mode for a simulation of a long-lived magnetized neutron star merger described by the APR4 EOS and masses $1.35 + 1.35\ M_\odot$. This model is slightly more massive than the one with the same EOS used in this work. The simulation is followed up to ≈100 ms after merger. This figure shows the presence of an unphysical gauge mode with a frequency of ≈1 kHz around 70 ms after merger. On the other hand the spectrogram shown in the bottom panel of their Fig. 16 displays the presence of a single mode up to 30 ms after merger while two modes become visible at a later time. This suggests a similar situation to the one described in the present work. Indeed, while [119] do not arrive at an explanation for this second frequency, they notice the similarity to our results in [32]. We note, however, that an unambiguous comparison would only be possible by extracting the associated eigenfunctions of the late-time modes found by [119].

Appendix B of [115] presents a study of convergence for a model very similar to the one discussed in the present work, namely a model with EOS SLy4 and masses $1.30 + 1.30\ M_\odot$. We recall that here we have considered a model described by the piecewise-polytropic representation of the SLy EOS with masses $1.28 + 1.28\ M_\odot$. The resolutions used by [115] are $dx = 415$ m (VLR), 246 m (LR), 185 m (SR), and 136 m (HR). The GW strain and time-frequency diagram are shown in their Fig. 13. In the postmerger phase the convergence properties of their simulations are poor (they had to use a rather small Courant-Friedrichs-Lewy factor of 0.075) with the VLR and SR simulations behaving differently to the LR run. Moreover, their HR simulation shows the formation of a black hole within less that 30 ms after merger (while this does not happen at the other resolutions) and that the phase of the waveform is not in the convergent regime. Nevertheless, the visual inspection of their results at VLR and SR resolutions seem compatible with our results. The discrepancy might be resolved by a closer examination of the numerical data of [115].

Finally [44] present a study of convectively unstable rotating neutron stars with nonbarotropic thermal profiles (as in the case of binary neutron star remnants). In their simulations, the thermal gradients naturally trigger convective motions in the star and the authors estimate [see their Eq. (C8)] that the growth timescale of convection is of order tens of ms close to the center, but reduces to the order of 0.1 ms at lower densities (close to the surface in their models). As [44] note referring to the rapid growth of convective instabilities in our simulations in the low-density envelope of the remnant, these timescales are compatible with those we find in [32] (and here). This is additional evidence in favor of our explanation of the late postmerger phase in our simulations.

APPENDIX C: PIECEWISE POLYTROPIC EOS

The numerical simulation of gravitational systems that include neutron stars requires a description of the behavior of matter at the very high density involved inside such compact objects. A full description would require a detailed understanding of the properties of matter at densities exceeding nuclear density, which is not yet fully accomplished. For this reason and for computational convenience, we here choose to model thermal effects similar to an ideal fluid. In this approximation, the energy momentum tensor is written as $T^{\mu\nu} = [\rho(1+\epsilon) + p]u^\mu u^\nu + p g^{\mu\nu}$ where ρ is the baryon density, ϵ is the specific internal energy and p is the pressure. As a consequence, the energy density is

$e = \rho(1+\epsilon)$. At this point, the thermal description of the system is achieved assuming (where $\epsilon_{\rm th}$ is an arbitrary function of thermodynamical state that has the properties of being zero at zero temperature):

$$\epsilon = \epsilon_0(\rho) + \epsilon_{\rm th}, \tag{C1}$$

$$p = p_0(\rho) + (\Gamma_{\rm th} - 1)\rho\epsilon_{\rm th}, \tag{C2}$$

and $\epsilon_0(\rho)$ and $p_0(\rho)$ are the specific internal energy and pressure at $T = 0$. For a fixed number of fermions the volume is $V = (1/\rho)$, and the energy $E = e/\rho$. The first law of thermodynamics is

$$dQ = dE + pdV = TdS. \tag{C3}$$

Assuming thermodynamic consistency, Eq. (C3), Frobenius theorem uniquely fixes (up to an arbitrary function, i.e., any function $\Sigma(s)$ gives other possible definitions of "temperature" and "entropy" (s,t) as $S = \Sigma(s)$ and $T = t/(d\Sigma(s)/ds)$) the "temperature"-like and "entropy"-like function as:

$$T = (\Gamma_{\rm th} - 1)\epsilon_{\rm th}, \tag{C4}$$

$$S = \log\left[\frac{(\epsilon_{\rm th})^{1/(\Gamma_{\rm th}-1)}}{\alpha\rho}\right], \tag{C5}$$

where α is an arbitrary constant with dimensions of the inverse of density. The conversion factor from the above dimensionless "temperature"-like values $\epsilon_{\rm th}$ and the real temperature T is given by the specific heat at constant volume and the function $\Sigma(s)$. The choice of $(\Sigma(s) = s)$ corresponds to having an "ideal-fluid" thermal behavior, and, as discussed in [120], the dimension of the temperature T can be found by multiplying Eq. (C4) by a factor m/k_B, where m is the value of the baryon mass. At the same time, the condition of thermodynamic consistency at $T = 0$ determines the functional relation between $\epsilon_0(\rho)$ and $p_0(\rho)$ ($dQ = 0$ at $T = 0$) that reads:

$$p_0(\rho) = \rho^2 \frac{d\epsilon_0(\rho)}{d\rho}. \tag{C6}$$

The zero-temperature piecewise polytropic approximate EOS amounts to the assumption that $p_0(\rho)$ and $\epsilon_0(\rho)$ are continuous polytropic functions of ρ. These conditions, and Equation (C6) imply that $p_0(\rho)$ and $\epsilon_0(\rho)$ are locally of the type:

$$\begin{aligned} p_0(\rho) &= K_i\rho^{\Gamma_i} \\ \epsilon_0(\rho) &= \epsilon_i + \frac{K_i}{\Gamma_i - 1}\rho^{\Gamma_i - 1} \end{aligned} \tag{C7}$$

and all coefficients are set once the polytropic index Γ_i $(i = 0, \ldots, N-1)$, the transition density ρ_i $(i = 1, \ldots, N-1)$ and K_0 are chosen. This defines an N-piece piecewise polytropic EOS with an "ideal-fluid" thermal component.

The specific enthalpy, in turn, is given by:

$$\begin{aligned} h = \frac{e+p}{\rho} &= \frac{(1+\epsilon)\rho + p}{\rho} \\ &= 1 + (1-\Gamma_i)\epsilon_i + \Gamma_{\rm th}\epsilon_{\rm th} + \Gamma_i\epsilon_0(\rho). \end{aligned} \tag{C8}$$

Since the relativistic speed of sound can be written as

$$\begin{aligned} c_s^2 = \frac{1}{h}\left(\frac{dp}{d\rho}\right)_s &= \frac{1}{h}\left[\left(\frac{\partial p}{\partial \rho}\right)_\epsilon + \frac{d\epsilon}{d\rho}\left(\frac{\partial p}{\partial \epsilon}\right)_\rho\right] \\ &= \frac{1}{h}\left[\left(\frac{\partial p}{\partial \rho}\right)_\epsilon + \frac{p}{\rho^2}\left(\frac{\partial p}{\partial \epsilon}\right)_\rho\right], \end{aligned} \tag{C9}$$

for a piecewise polytropic EOS we have:

$$c_s^2 = \frac{\Gamma_{\rm th}(\Gamma_{\rm th}-1)\epsilon_{\rm th} + \Gamma_i(\Gamma_i - 1)(\epsilon_0(\rho) - \epsilon_i)}{1 + (1-\Gamma_i)\epsilon_i + \Gamma_{\rm th}\epsilon_{\rm th} + \Gamma_i\epsilon_0(\rho)}$$

where ϵ_0 is the same as in Equation (C7) and the index i refers to the ith piece. At the transition point we have imposed the condition that the pressure and energy density are continuous, but that does not hold true for the speed of sound that can be discontinuous, i.e., in general $(c_s^2)_i(\rho_i) \neq (c_s^2)_{i+1}(\rho_i)$.

For a piecewise polytropic EOS we calculate the adiabatic index (Γ_1) for adiabatic perturbations as:

$$\begin{aligned} \Gamma_1 = \frac{e+p}{p}\left(\frac{dp}{de}\right)_s &= \left(\frac{d\ln p}{d\ln\rho}\right)_s \\ &= \Gamma_{\rm th} + (\Gamma_i - \Gamma_{\rm th})\frac{K_i\rho^{\Gamma_i}}{p} \end{aligned} \tag{C10}$$

where ϵ is the specific internal energy, K_i and Γ_i are the polytropic constant and exponent in the ith piece of the EOS.

The construction presented here has been considered as a 2D equation of state in [44]. They chose to assume as "entropy" the quantity s defined by $S = \Sigma(s) = 2/(\Gamma_{\rm th} - 1)\log(s)$ and to fix the value of the constant α so that it corresponds to having $\epsilon_{\rm th} \propto s^2\rho^{\Gamma_{\rm th}-1}$. Indeed we should expect, as shown in [44], that nonbarotropic stellar configurations (including binary neutron star merger remnants) may be subject to convective instabilities.

Another possibility is to assume as "entropy" the quantity s defined by $S = \Sigma(s) = \log(s)$. With this choice the expressions for the main thermodynamical variables, as function of ρ and s, are

$$\epsilon = \epsilon_0(\rho) + s^{\Gamma_{\rm th}-1}\cdot(\alpha\rho)^{\Gamma_{\rm th}-1} \tag{C11}$$

$$p = p_0(\rho) + (\Gamma_{\rm th} - 1) \cdot \rho \cdot s^{\Gamma_{\rm th}-1} \cdot (\alpha\rho)^{\Gamma_{\rm th}-1} \tag{C12}$$

$$t = (\Gamma_{\rm th} - 1) \cdot s^{\Gamma_{\rm th}-2} \cdot (\alpha\rho)^{\Gamma_{\rm th}-1}. \tag{C13}$$

One should note that this choice is of difficult physical interpretation in the case of $\Gamma_{\rm th} = 2$ since it would imply that we should interpret the density as the temperature of the system. The "entropy" (s) and the "temperature" (t) in terms of the internal energy and density are expressed by:

$$\epsilon_{\rm th} = (\epsilon - \epsilon_0(\rho)) \tag{C14}$$

$$t = (\Gamma_{\rm th} - 1) \cdot (\epsilon_{\rm th})^{(\Gamma_{\rm th}-2)/(\Gamma_{\rm th}-1)} \cdot (\alpha\rho) \tag{C15}$$

$$s = (\epsilon_{\rm th})^{1/(\Gamma_{\rm th}-1)}/(\alpha\rho) \tag{C16}$$

$$t \cdot s = (\epsilon_{\rm th}) \tag{C17}$$

This concludes the discussion of the thermodynamic proprieties of the EOSs used in the present work.

[1] B. P. Abbott, R. Abbott, T. D. Abbott, F. Acernese, K. Ackley, C. Adams, T. Adams, P. Addesso, R. X. Adhikari, V. B. Adya *et al.*, Astrophys. J. Lett. **848**, L12 (2017).
[2] B. P. Abbott, R. Abbott, T. D. Abbott, F. Acernese, K. Ackley, C. Adams, T. Adams, P. Addesso, R. X. Adhikari, V. B. Adya *et al.*, Astrophys. J. Lett. **848**, L13 (2017).
[3] D. Kasen, B. Metzger, J. Barnes, E. Quataert, and E. Ramirez-Ruiz, Nature (London) **551**, 80 (2017).
[4] B. P. Abbott, R. Abbott, T. D. Abbott, F. Acernese, K. Ackley, C. Adams, T. Adams, P. Addesso, R. X. Adhikari, V. B. Adya *et al.*, Nature (London) **551**, 85 (2017).
[5] E. Pian *et al.*, Nature (London) **551**, 67 (2017).
[6] B. P. Abbott, R. Abbott, T. D. Abbott, F. Acernese, K. Ackley, C. Adams, T. Adams, P. Addesso, R. X. Adhikari, V. B. Adya *et al.*, Phys. Rev. Lett. **119**, 161101 (2017).
[7] B. P. Abbott *et al.* (LIGO Scientific and Virgo Collaborations), arXiv:1805.11579.
[8] B. P. Abbott *et al.* (LIGO Scientific and Virgo Collaborations), Phys. Rev. Lett. **121**, 161101 (2018).
[9] S. De, D. Finstad, J. M. Lattimer, D. A. Brown, E. Berger, and C. M. Biwer, Phys. Rev. Lett. **121**, 091102 (2018).
[10] F. J. Fattoyev, J. Piekarewicz, and C. J. Horowitz, Phys. Rev. Lett. **120**, 172702 (2018).
[11] E. Annala, T. Gorda, A. Kurkela, and A. Vuorinen, Phys. Rev. Lett. **120**, 172703 (2018).
[12] P. B. Abbott *et al.* (LIGO Scientific and Virgo Collaborations), Classical Quantum Gravity **37**, 045006 (2020).
[13] I. Tews, J. Margueron, and S. Reddy, AIP Conf. Proc. **2127**, 020009 (2019).
[14] Z. Carson, A. W. Steiner, and K. Yagi, Phys. Rev. D **100**, 023012 (2019).
[15] B. Margalit and B. D. Metzger, Astrophys. J. Lett. **880**, L15 (2019).
[16] A. Bauswein, O. Just, H.-T. Janka, and N. Stergioulas, Astrophys. J. Lett. **850**, L34 (2017).
[17] A. Bauswein and N. Stergioulas, J. Phys. G **46**, 113002 (2019).
[18] L. Baiotti, arXiv:1907.08534.
[19] M. Shibata and K. Uryū, Prog. Theor. Phys. **107**, 265 (2002).
[20] M. Shibata, Phys. Rev. Lett. **94**, 201101 (2005).
[21] N. Stergioulas, A. Bauswein, K. Zagkouris, and H.-T. Janka, Mon. Not. R. Astron. Soc. **418**, 427 (2011).
[22] A. Bauswein and H. T. Janka, Phys. Rev. Lett. **108**, 011101 (2012).
[23] A. Bauswein, H. T. Janka, K. Hebeler, and A. Schwenk, Phys. Rev. D **86**, 063001 (2012).
[24] A. Bauswein and N. Stergioulas, Phys. Rev. D **91**, 124056 (2015).
[25] J. A. Clark, A. Bauswein, N. Stergioulas, and D. Shoemaker, Classical Quantum Gravity **33**, 085003 (2016).
[26] A. Bauswein, N.-U. F. Bastian, D. B. Blaschke, K. Chatziioannou, J. A. Clark, T. Fischer, and M. Oertel, Phys. Rev. Lett. **122**, 061102 (2019).
[27] A. Torres-Rivas, K. Chatziioannou, A. Bauswein, and J. A. Clark, Phys. Rev. D **99**, 044014 (2019).
[28] A. Bauswein, N. Stergioulas, and H.-T. Janka, Eur. Phys. J. A **52**, 56 (2016).
[29] K. Chatziioannou, J. A. Clark, A. Bauswein, M. Millhouse, T. B. Littenberg, and N. Cornish, Phys. Rev. D **96**, 124035 (2017).
[30] S. Bose, K. Chakravarti, L. Rezzolla, B. S. Sathyaprakash, and K. Takami, Phys. Rev. Lett. **120**, 031102 (2018).
[31] H. Yang, V. Paschalidis, K. Yagi, L. Lehner, F. Pretorias, and N. Yunes, Phys. Rev. D **97**, 024049 (2018).
[32] R. De Pietri, A. Feo, J. A. Font, F. Löffler, F. Maione, M. Pasquali, and N. Stergioulas, Phys. Rev. Lett. **120**, 221101 (2018).
[33] M. D. Duez, Classical Quantum Gravity **27**, 114002 (2010).
[34] J. A. Faber and F. A. Rasio, Living Rev. Relativity **15**, 8 (2012).
[35] V. Paschalidis, Classical Quantum Gravity **34**, 084002 (2017).
[36] L. Baiotti and L. Rezzolla, Rep. Prog. Phys. **80**, 096901 (2017).
[37] T. W. Baumgarte, S. L. Shapiro, and M. Shibata, Astrophys. J. **528**, L29 (2000).
[38] G. Cook, S. Shapiro, and S. Teukolsky, Astrophys. J. **398**, 203 (1992).
[39] S. Chandrasekhar, Phys. Rev. Lett. **24**, 611 (1970).

[40] J. L. Friedman and B. F. Schutz, Astrophys. J. **222**, 281 (1978).
[41] A. L. Watts, N. Andersson, H. R. Beyer, and B. F. Schutz, Mon. Not. R. Astron. Soc. **342**, 1156 (2003).
[42] A. L. Watts, N. Andersson, and D. I. Jones, Astrophys. J. **618**, L37 (2005).
[43] G. Corvino, L. Rezzolla, S. Bernuzzi, R. De Pietri, and B. Giacomazzo, Classical Quantum Gravity **27**, 114104 (2010).
[44] G. Camelio, T. Dietrich, M. Marques, and S. Rosswog, Phys. Rev. D **100**, 123001 (2019).
[45] B. P. Abbott, R. Abbott, T. D. Abbott, F. Acernese, K. Ackley, C. Adams, T. Adams, P. Addesso, R. X. Adhikari, V. B. Adya *et al.*, Astrophys. J. Lett. **851**, L16 (2017).
[46] B. P. Abbott *et al.* (LIGO Scientific and Virgo Collaborations), Phys. Rev. X **9**, 011001 (2019).
[47] B. P. Abbott *et al.* (LIGO Scientific and Virgo Collaborations), Astrophys. J. **875**, 160 (2019).
[48] M. H. P. M. van Putten and M. Della Valle, Mon. Not. R. Astron. Soc. **482**, L46 (2019).
[49] X. Zhuge, J. M. Centrella, and S. L. W. McMillan, Phys. Rev. D **50**, 6247 (1994).
[50] M. Shibata and K. b. o. Uryū, Phys. Rev. D **61**, 064001 (2000).
[51] R. Oechslin, S. Rosswog, and F.-K. Thielemann, Phys. Rev. D **65**, 103005 (2002).
[52] M. Shibata, K. Taniguchi, and K. Uryū, Phys. Rev. D **71**, 084021 (2005).
[53] M. Shibata and K. Taniguchi, Phys. Rev. D **73**, 064027 (2006).
[54] K. Kiuchi, Y. Sekiguchi, M. Shibata, and K. Taniguchi, Phys. Rev. D **80**, 064037 (2009).
[55] K. Hotokezaka, K. Kiuchi, K. Kyutoku, T. Muranushi, Y.-i. Sekiguchi, M. Shibata, and K. Taniguchi, Phys. Rev. D **88**, 044026 (2013).
[56] K. Takami, L. Rezzolla, and L. Baiotti, Phys. Rev. D **91**, 064001 (2015).
[57] S. Bernuzzi, T. Dietrich, and A. Nagar, Phys. Rev. Lett. **115**, 091101 (2015).
[58] T. Dietrich, S. Bernuzzi, M. Ujevic, and B. Brügmann, Phys. Rev. D **91**, 124041 (2015).
[59] T. Dietrich, S. Bernuzzi, M. Ujevic, and W. Tichy, Phys. Rev. D **95**, 044045 (2017).
[60] T. Dietrich, M. Ujevic, W. Tichy, S. Bernuzzi, and B. Bruegmann, Phys. Rev. D **95**, 024029 (2017).
[61] L. Rezzolla and K. Takami, Phys. Rev. D **93**, 124051 (2016).
[62] L. Lehner, S. L. Liebling, C. Palenzuela, O. L. Caballero, E. O'Connor, M. Anderson, and D. Neilsen, Classical Quantum Gravity **33**, 184002 (2016).
[63] F. Maione, R. De Pietri, A. Feo, and F. Löffler, Phys. Rev. D **96**, 063011 (2017).
[64] L. Baiotti, Prog. Part. Nucl. Phys. **109**, 103714 (2019).
[65] L. Baiotti, B. Giacomazzo, and L. Rezzolla, Phys. Rev. D **78**, 084033 (2008).
[66] M. Anderson, E. W. Hirschmann, L. Lehner, S. L. Liebling, P. M. Motl, D. Neilsen, C. Palenzuela, and J. E. Tohline, Phys. Rev. D **77**, 024006 (2008).
[67] Y. T. Liu, S. L. Shapiro, Z. B. Etienne, and K. Taniguchi, Phys. Rev. D **78**, 024012 (2008).
[68] W. Kastaun and F. Galeazzi, Phys. Rev. D **91**, 064027 (2015).
[69] R. De Pietri, A. Feo, F. Maione, and F. Löffler, Phys. Rev. D **93**, 064047 (2016).
[70] W. Kastaun, R. Ciolfi, and B. Giacomazzo, Phys. Rev. D **94**, 044060 (2016).
[71] V. Paschalidis, W. E. East, F. Pretorius, and S. L. Shapiro, Phys. Rev. D **92**, 121502 (2015).
[72] W. E. East, V. Paschalidis, and F. Pretorius, Classical Quantum Gravity **33**, 244004 (2016).
[73] M. Hanauske, K. Takami, L. Bovard, L. Rezzolla, J. A. Font, F. Galeazzi, and H. Stocker, Phys. Rev. D **96**, 043004 (2017).
[74] F. Foucart, R. Haas, M. D. Duez, E. O'Connor, C. D. Ott, L. Roberts, L. E. Kidder, J. Lippuner, H. P. Pfeiffer, and M. A. Scheel, Phys. Rev. D **93**, 044019 (2016).
[75] M. Shibata and K. Kiuchi, Phys. Rev. D **95**, 123003 (2017).
[76] S. Fujibayashi, K. Kiuchi, N. Nishimura, Y. Sekiguchi, and M. Shibata, Astrophys. J. **860**, 64 (2018).
[77] LORENE, LORENE: Langage objet pour la RElativité NumériquE, http://www.lorene.obspm.fr/.
[78] E. Gourgoulhon, P. Grandclement, K. Taniguchi, J.-A. Marck, and S. Bonazzola, Phys. Rev. D **63**, 064029 (2001).
[79] J. S. Read, B. D. Lackey, B. J. Owen, and J. L. Friedman, Phys. Rev. D **79**, 124032 (2009).
[80] F. Löffler, J. Faber, E. Bentivegna, T. Bode, P. Diener, R. Haas, I. Hinder, B. C. Mundim, C. D. Ott, E. Schnetter, G. Allen, M. Campanelli, and P. Laguna, Classical Quantum Gravity **29**, 115001 (2012).
[81] Cactus developers, Cactus Computational Toolkit, http://www.cactuscode.org/.
[82] T. Goodale, G. Allen, G. Lanfermann, J. Massó, T. Radke, E. Seidel, and J. Shalf, in *Vector and Parallel Processing —VECPAR'2002, 5th International Conference, Lecture Notes in Computer Science* (Springer, Berlin, 2003).
[83] F. Maione, R. De Pietri, A. Feo, and F. Löffler, Classical Quantum Gravity **33**, 175009 (2016).
[84] A. Feo, R. De Pietri, F. Maione, and F. Löffler, Classical Quantum Gravity **34**, 034001 (2017).
[85] R. De Pietri, A. Drago, A. Feo, G. Pagliara, M. Pasquali, S. Traversi, and G. Wiktorowicz, Astrophys. J. **881**, 122 (2019).
[86] M. Shibata and T. Nakamura, Phys. Rev. D **52**, 5428 (1995).
[87] T. W. Baumgarte and S. L. Shapiro, Phys. Rev. D **59**, 024007 (1998).
[88] McLachlan, McLachlan, a public BSSN code, http://www.cct.lsu.edu/~eschnett/McLachlan/.
[89] F. Banyuls, J. A. Font, J. M. Ibáñez, J. M. Martí, and J. A. Miralles, Astrophys. J. **476**, 221 (1997).
[90] J. A. Font, Living Rev. Relativity **11**, 7 (2008).
[91] L. Baiotti, I. Hawke, P. J. Montero, F. Löffler, L. Rezzolla, N. Stergioulas, J. A. Font, and E. Seidel, Phys. Rev. D **71**, 024035 (2005).
[92] P. Mösta, B. C. Mundim, J. A. Faber, R. Haas, S. C. Noble, T. Bode, F. Löffler, C. D. Ott, C. Reisswig, and E. Schnetter, Classical Quantum Gravity **31**, 015005 (2014).
[93] A. Harten, P. D. Lax, and B. van Leer, SIAM Rev. **25**, 35 (1983).

[94] B. Einfeldt, Numer. Anal. **25**, 294 (1988).
[95] X.-D. Liu, S. Osher, and T. Chan, J. Comput. Phys. **115**, 200 (1994).
[96] G.-S. Jiang and C.-W. Shu, J. Comput. Phys. **126**, 202 (1996).
[97] C. Runge, Math. Ann. **46**, 167 (1895).
[98] W. Kutta, Z. Math. Phys. **46**, 435 (1901).
[99] F. Acernese *et al.* (Virgo Collaboration), Classical Quantum Gravity **32**, 024001 (2015).
[100] J. Aasi *et al.* (LIGO Scientific Collaboration), Classical Quantum Gravity **32**, 074001 (2015).
[101] M. Punturo *et al.*, Classical Quantum Gravity **27**, 194002 (2010).
[102] B. P. Abbott *et al.* (LIGO Scientific Collaboration), Classical Quantum Gravity **34**, 044001 (2017).
[103] K. D. Kokkotas and B. G. Schmidt, Living Rev. Relativity **2**, 2 (1999).
[104] N. Stergioulas, T. A. Apostolatos, and J. A. Font, Mon. Not. R. Astron. Soc. **352**, 1089 (2004).
[105] K. H. Lockitch and J. L. Friedman, Astrophys. J. **521**, 764 (1999).
[106] K. H. Lockitch, J. L. Friedman, and N. Andersson, Phys. Rev. D **68**, 124010 (2003).
[107] K. K. Zhang and F. H. Busse, Geophys. Astrophys. Fluid Dyn. **39**, 119 (1987).
[108] R. Simitev and F. H. Busse, New J. Phys. **5**, 97 (2003).
[109] F. H. Busse and R. Simitev, J. Fluid Mech. **498**, 23 (2004).
[110] K. Zhang and X. Liao, *Theory and Modeling of Rotating Fluids: Convection, Inertial Waves and Precession* (Cambridge University Press, Cambridge, England, 2017), pp. 1–540.
[111] M. Shibata and K. Taniguchi, Phys. Rev. D **73**, 064027 (2006).
[112] L. Baiotti, R. De Pietri, G. M. Manca, and L. Rezzolla, Phys. Rev. D **75**, 044023 (2007).
[113] R. De Pietri, A. Feo, L. Franci, and F. Löffler, Phys. Rev. D **90**, 024034 (2014).
[114] F. Löffler, R. De Pietri, A. Feo, F. Maione, and L. Franci, Phys. Rev. D **91**, 064057 (2015).
[115] M. Breschi, S. Bernuzzi, F. Zappa, M. Agathos, A. Perego, D. Radice, and A. Nagar, Phys. Rev. D **100**, 104029 (2019).
[116] L. Rezzolla, L. Baiotti, B. Giacomazzo, D. Link, and J. A. Font, Classical Quantum Gravity **27**, 114105 (2010).
[117] N. Andersson *et al.*, Classical Quantum Gravity **30**, 193002 (2013).
[118] X. Zhang, Z. Cao, and H. Gao, Int. J. Mod. Phys. D **28**, 1950026 (2019).
[119] R. Ciolfi, W. Kastaun, J. V. Kalinani, and B. Giacomazzo, Phys. Rev. D **100**, 023005 (2019).
[120] L. Rezzolla and O. Zanotti, *Relativistic Hydrodynamics, EBSCO ebook Academic Collection* (Oxford University Press, Oxford, 2013).